



**HAL**  
open science

**Fingerprinting stress: Stylolite and calcite twinning  
paleopiezometry revealing the complexity of progressive  
stress patterns during folding - The case of the Monte  
Nero anticline in the Apennines, Italy**

Nicolas Beaudoin, Daniel Koehn, Olivier Lacombe, Alexandre Lecouty,  
Andrea Billi, Einat Aharonov, Camille Parlangeau

► **To cite this version:**

Nicolas Beaudoin, Daniel Koehn, Olivier Lacombe, Alexandre Lecouty, Andrea Billi, et al.. Fingerprinting stress: Stylolite and calcite twinning paleopiezometry revealing the complexity of progressive stress patterns during folding - The case of the Monte Nero anticline in the Apennines, Italy. *Tectonics*, 2016, 35 (7), pp.1687-1712 10.1002/2016TC004128 . hal-01393352

**HAL Id: hal-01393352**

**<https://hal.science/hal-01393352>**

Submitted on 21 Nov 2016

**HAL** is a multi-disciplinary open access archive for the deposit and dissemination of scientific research documents, whether they are published or not. The documents may come from teaching and research institutions in France or abroad, or from public or private research centers.

L'archive ouverte pluridisciplinaire **HAL**, est destinée au dépôt et à la diffusion de documents scientifiques de niveau recherche, publiés ou non, émanant des établissements d'enseignement et de recherche français ou étrangers, des laboratoires publics ou privés.



## Tectonics

### RESEARCH ARTICLE

10.1002/2016TC004128

#### Key Points:

- New combination of stylolites and calcite twins inversion as stress indicator during folding
- Reconstruction of complex stress regime oscillation during fold growth
- Use of deep sedimentary stylolite gives high resolution access to local burial history

#### Correspondence to:

N. Beaudoin,  
Nicolas.Beaudoin@glasgow.ac.uk

#### Citation:

Beaudoin, N., D. Koehn, O. Lacombe, A. Lecouty, A. Billi, E. Aharonov, and C. Parlangau (2016), Fingerprinting stress: Stylolite and calcite twinning paleopiezometry revealing the complexity of progressive stress patterns during folding—The case of the Monte Nero anticline in the Apennines, Italy, *Tectonics*, 35, 1687–1712, doi:10.1002/2016TC004128.

Received 15 JAN 2016

Accepted 15 JUN 2016

Accepted article online 20 JUN 2016

Published online 19 JUL 2016

## Fingerprinting stress: Stylolite and calcite twinning paleopiezometry revealing the complexity of progressive stress patterns during folding—The case of the Monte Nero anticline in the Apennines, Italy

Nicolas Beaudoin<sup>1</sup>, Daniel Koehn<sup>1</sup>, Olivier Lacombe<sup>2</sup>, Alexandre Lecouty<sup>2</sup>, Andrea Billi<sup>3</sup>, Einat Aharonov<sup>4</sup>, and Camille Parlangau<sup>2</sup>

<sup>1</sup>School of Geographical and Earth Sciences, University of Glasgow, Glasgow, UK, <sup>2</sup>Institut des Sciences de la Terre de Paris, Sorbonne Universités, UPMC Université Paris 06, CNRS, Paris, France, <sup>3</sup>IGAG, Consiglio Nazionale delle Ricerche, Rome, Italy, <sup>4</sup>Institute of Earth Sciences, Hebrew University of Jerusalem, Jerusalem, Israel

**Abstract** In this study we show for the first time how quantitative stress estimates can be derived by combining calcite twinning and stylolite roughness stress fingerprinting techniques in a fold-and-thrust belt. First, we present a new method that gives access to stress inversion using tectonic stylolites without access to the stylolite surface and compare results with calcite twin inversion. Second, we use our new approach to present a high-resolution deformation and stress history that affected Meso-Cenozoic limestone strata in the Monte Nero Anticline during its late Miocene-Pliocene growth in the Umbria-Marche Arcuate Ridge (northern Apennines, Italy). In this area an extensive stylolite-joint/vein network developed during layer-parallel shortening (LPS), as well as during and after folding. Stress fingerprinting illustrates how stress in the sedimentary strata did build up prior to folding during LPS. The stress regime oscillated between strike slip and compressional during LPS before ultimately becoming strike slip again during late stage fold tightening. Our case study shows that high-resolution stress fingerprinting is possible and that this novel method can be used to unravel temporal relationships that relate to local variations of regional orogenic stresses. Beyond regional implications, this study validates our approach as a new powerful toolbox to high-resolution stress fingerprinting in basins and orogens combining joint and vein analysis with sedimentary and tectonic stylolite and calcite twin inversion techniques.

### 1. Introduction

An understanding of the spatiotemporal distribution of stresses in the Earth's crust is important for applied geological problems such as hazard studies, engineering, and resource exploration. From a more fundamental point of view, stresses are important to understand the dynamics of geological systems on all scales from plate tectonics down to microstructures. For example, constraining paleostresses in fold-and-thrust belts and sedimentary basins allows reconstruction of both local and regional geological histories and leads to a better description of fluid flow and reservoir evolution. Studies of distributed, subseismic fractures have led to a better understanding of how mesostructures can record local to regional deformation sequences and consequently capture the paleostress history [Stearns and Friedman, 1972; Engelder, 1987; Laubach, 1988, 1989; Fischer et al., 1992; Cooke, 1997; Saintot et al., 2003; Bergbauer and Pollard, 2004; Laubach et al., 2004; Bellahsen et al., 2006a, 2006b; Cooper et al., 2006; Tavani et al., 2012, 2015; Ahmadhadi et al., 2007, 2008; Amrouch et al., 2010; Savage et al., 2010; Casini et al., 2011; Lacombe et al., 2011; Beaudoin et al., 2012; among others].

Many projects aim at monitoring current stress levels in the Earth's crust by using piezometers in boreholes or looking at the seismological records, which is, for example, recorded in the world stress map [Heidbach et al., 2007]. However, in order to have a comprehensive view of longer-term effects of stress on rocks, paleopiezometers have been developed since the 1980s [Jamison and Spang, 1976; Kohlstedt and Weathers, 1980; Etchecopar, 1984; Angelier, 1989; Lacombe and Laurent, 1992]. Inversion techniques applied on mesostructure/microstructure like striated fault planes or calcite twins illustrate how stress regimes and differential stresses evolve at the regional scale in orogenic forelands or at a more local scale through the formation of structures like folds [Michael, 1984; Lacombe et al., 1990, 1996, 2007; Rocher et al., 1996, 2000;

Lacombe, 2001; André *et al.*, 2001; Orife and Lisle, 2003, 2006; Amrouch *et al.*, 2010, 2011; Beaudoin *et al.*, 2012]. The development of paleopiezometric techniques resulted in refined models that link deformation and stress histories. However, the use of such tools is not systematic, mainly because of the complexity of the signal acquisition and inversion process and because uncertainties persist over the magnitude of stress reconstructed [e.g., Lacombe, 2007, 2010]. Stress studies of folding have paid little attention to pressure-solution even though it is a widely acknowledged mechanism of deformation in the upper crust [Stockdale, 1943; Alvarez *et al.*, 1976; Engelder *et al.*, 1981; Gratier and Guiguet *Irigm*, 1986; Railsback, 1993; Gratier *et al.*, 2005].

Common pressure-solution features are stylolites [Alvarez *et al.*, 1978], which develop rough surfaces and look like sutures in outcrop walls. Stylolites are common deformation features especially in carbonate rocks, and they are important because up to 50% of the initial rock volume can be dissolved at these surfaces [Alvarez *et al.*, 1978] and they strongly impact fault development [Marshak *et al.*, 1982; Gratier *et al.*, 2003; Tondi *et al.*, 2006; Faulkner *et al.*, 2010]. In recent years, stylolites were included in the reconstruction of fold histories in addition to the classical use of fracture and fault patterns [e.g., Tavani *et al.*, 2008, 2015; Petracchini *et al.*, 2012]. In addition, their impact on reservoir properties is debated [Heap *et al.*, 2014]. Recent understanding of the growth mechanism of stylolites during burial and contraction has led to the proposition of a new paleopiezometer based on the stylolite roughness [Renard *et al.*, 2004; Schmittbuhl *et al.*, 2004; Koehn *et al.*, 2007, 2012; Ebner *et al.*, 2010a, 2010b; Rolland *et al.*, 2012, 2014]. So far, this method is not often mentioned in tectonic studies, because the paleopiezometer was mainly used to reconstruct the maximum depth of burial of a formation using bedding-parallel stylolites [Ebner *et al.*, 2009, 2010b; Rolland *et al.*, 2014]. One study, however, has shown that tectonic stylolites can be used to reconstruct the stress magnitude of rocks under the condition that the tectonic stylolite roughness is investigated in 3-D on open stylolite planes [Ebner *et al.*, 2010a]. Published results for stylolite paleopiezometry support that the stress magnitudes reconstructed are robust for shallow depth deformation (<1000 m). Several works show statistically that stylolites grow according to physical laws described by Schmittbuhl *et al.* [2004], and so by applying a proper method for data selection, acquisition, and treatment, one can consider a stylolite population as a good proxy for stress related to vertical or horizontal compaction [e.g., Koehn *et al.*, 2007; Ebner *et al.*, 2009, 2010a, 2010b; Rolland *et al.*, 2012, 2014]. Previous papers caution, however, that paleopiezometry based on stylolite roughness inversion only can contain uncertainties, because of the timing of stylolite growth and nonnegligible uncertainties as a function of stylolite morphologies [Rolland *et al.*, 2014].

This contribution reports the reconstruction of the evolution of paleostress orientation and magnitude prevailing in sedimentary strata during the entire history of an anticline structure, from prefolding/early folding layer-parallel shortening (LPS) to late-stage fold-tightening and postfolding evolution. To do so, we combine for the first time a study of extensional fracture and stylolite network orientation and age relationships at fold-scale with calcite twinning and stylolite roughness paleopiezometry. The study focuses on the Monte Nero Anticline, located in the Umbria-Marche Arcuate Ridge, northern Apennines, Italy (Figure 1). The sequence of deformation is constrained by the development of successive sets of mesostructures (mainly fractures) predating, coeval with and postdating folding. This sequence is used as a relative timeframe wherein paleostress tensors are reconstructed from independent inversion of calcite twins and tectonic stylolite 3-D roughness. The maximum burial depth is reconstructed from the inversion of the roughness of bedding-parallel stylolites. The combined data set is used to reconstruct a high-resolution stress evolution of the folded sequence. We propose a new method to overcome the challenge of having to use open stylolite surfaces for tectonic stylolite paleopiezometry. We demonstrate that stress fingerprinting of stylolites can provide reliable quantitative data for the progressive stress evolution of folded and fractured sedimentary carbonate rocks in a fold-and-thrust belt. The reported new combination of stress fingerprinting methods offers a so-far unknown insight into the tectonic evolution of the past.

## 2. Geological Setting

The Monte Nero Anticline (MNA) gathers the local highs of Monte Nero, Monte Penna, and Monte Serra Santa that belong to the Umbria-Marche Arcuate Ridge (UMAR) in the northern Apennines fold-and-thrust belt [Lavecchia *et al.*, 1988; Carminati *et al.*, 2010] (Figure 1). The UMAR is a tectonically active (presently undergoing postorogenic extension) region comprising a succession of NNW-SSE trending arcuate folds and

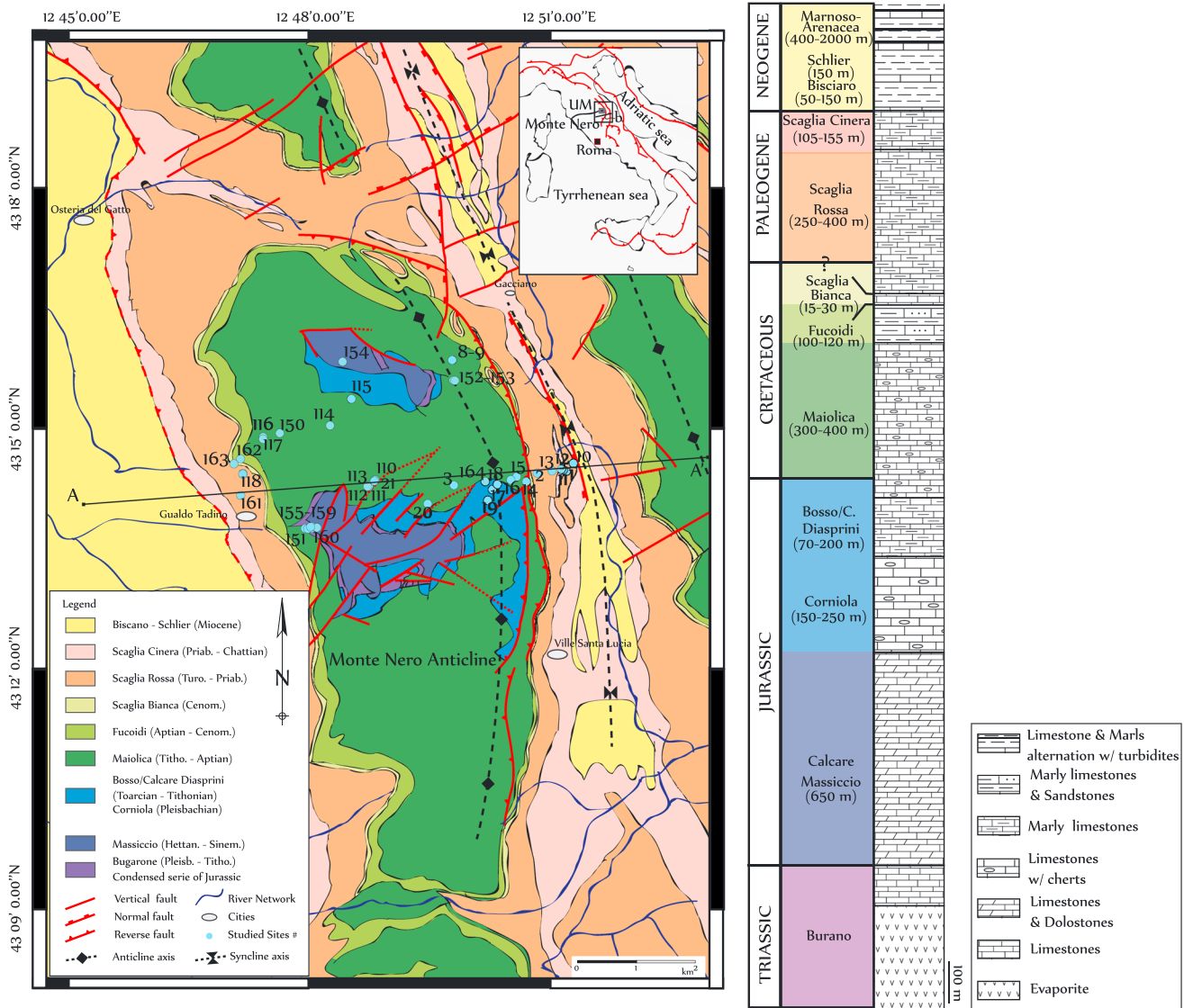


**Figure 1.** (a) Simplified geological map of the Monte Nero area after *Jacobacci* [1979]. Line A-A' refers to the cross section from Figure 2a. (b) Stratigraphic column of the Monte Nero area, after *Jacobacci* [1979].

thrusts developed with a general eastward piggyback sequence [*Bally et al.*, 1986; *Calamita and Deiana*, 1988; *Barchi et al.*, 2012]. The region underwent E-W extension related to Liassic rifting, followed by NE-SW compression associated with the Apenninic orogeny that started by Tortonian times in the study area [*Barchi et al.*, 2012]. The northern Apennines belt is now experiencing a postorogenic extension perpendicular to the range in the axial and innermost structures, while the orogenic compression keeps being active toward the east in the Adriatic domain. Map-view rotation history of the UMAR is not well constrained because of its complicated tectonic history, yet the UMAR as a belt is interpreted as an orocline, i.e., with no significant map view rotation [*Lowrie and Hist*, 1988; *Channell*, 1992; *Speranza et al.*, 1997; *Van Hinsbergen et al.*, 2014].

The MNA is an arcuate anticline with a gentle backlimb dipping 30° toward W-SW and a forelimb with secondary folds and with locally overturned strata. The MNA likely formed during the Tortonian when the western part of the UMAR switched from foredeep basin to wedge-top basin and likely emerged during the Messinian [*Elter et al.*, 1975; *Scarselli et al.*, 2007; *Tavani et al.*, 2008; *Barchi et al.*, 2012]. Recent insights into the crustal structure of the UMAR provided by a crustal-scale seismic profile (CROP-03 [*Mirabella et al.*, 2008; *Barchi et al.*, 2012; *Scisciani et al.*, 2014], CROP 11 [*Billi et al.*, 2006]) show that the MNA is a pop-up structure formed by high-angle reverse faults in both limbs of the fold (Figure 2). These faults are visible on the CROP-03 seismic profile and are

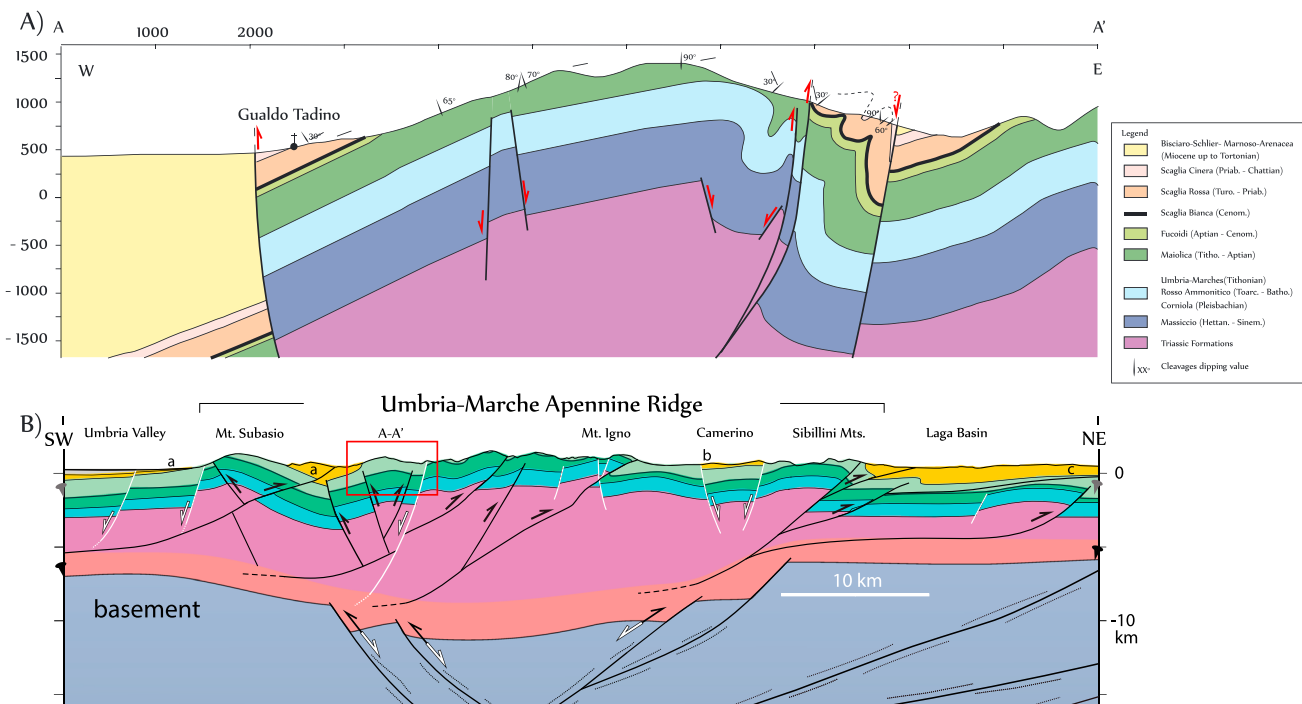


**Figure 2.** (a) Cross section along line A-A' (Figure 1) on which the measured tectonic cleavages are reported with dip values. (b) Balanced crustal cross section where basement deformation is decoupled with respect to the sedimentary cover. Red frame labelled A-A' is the southward equivalent of the Monte Nero [after Scisciani et al., 2014].

interpreted as soling downward into a large-scale west dipping thrust [Scisciani et al., 2014] (Figure 2b). The outermost (eastern) fault is mainly N-S striking in the south and changes to NW-SE toward the northern part of the fold (Figure 1a), which is mimicked by the gentle curvature of the hinge of the MNA in map view. The steep dip of the boundary reverse faults suggests that they resulted from the inversion of preexisting normal faults inherited from the Liassic rifting [Deiana et al., 2002], which is recorded by several normal faults in the Massiccio Fm. The extension of the latter normal faults into younger sediments suggests they were possibly reactivated during the later foreland bulging, folding, subsidence, or during the current extension [Marchegiani et al., 1999; Pizzi and Scisciani, 2000] (Figure 1). The current extensional stress configuration that is related to postorogenic collapse or back-arc extension is reflected in normal faults that cut a syncline located east to the MNA.

The competent local sedimentary succession that overlies Triassic anhydrites and dolostones (Anidridi di Burano Fm.) is the following [Martinis and Pieri, 1964; Jacobacci, 1979; Tavani et al., 2008; Pierantoni et al., 2013] (Figure 1b): (1) late Triassic limestones with marl intercalation; (2) massive dolomites of the Calcare Massiccio Fm. (Hettangian-Sinemurian); (3) grey Jurassic limestones with chert beds of the Corniola Fm. (Lothangian-Pleisbachian); (4) micritic limestones, marls, and cherts of the Bosso/Calcare Diasprini Fm (Toarcian-Tithonian); (5) white limestones with chert beds of the Maiolica Fm. (Tithonian-Aptian); (6) marly limestones of the Fucoidi Fm. (Aptian-Cenomanian); (7) white marly limestones of the Scaglia Bianca Fm. (Cenomanian); (8) pink marly limestones of the Scaglia Rossa Fm. (Turonian-Priabonian); and (9) grey marly limestones of the Scaglia Cinera Fm. (Priabonian- Chattian). Up to 3000 m of Miocene sediments deposited on top of this formation, when the area was forming as part of the foredeep ahead of the advancing fold-and-thrust belt, including clay-rich limestones and silts of the Bisciario Fm. and of the Schlier Fm. (Aquitanian-Tortonian).

### 3. Methods

#### 3.1. History of Deformation From Fracture and Stylolite Analysis

Mesostructures were measured and sampled in different accessible formations along a N090 and a N060 trending (all directions are given toward east) section across the MNA. The formations have very variable stylolite distributions, poor stylolite sets in the massive carbonate of the Calcare Massiccio Fm., and well-expressed pressure-solution features in other strata [Alvarez et al., 1978], especially the marly carbonates



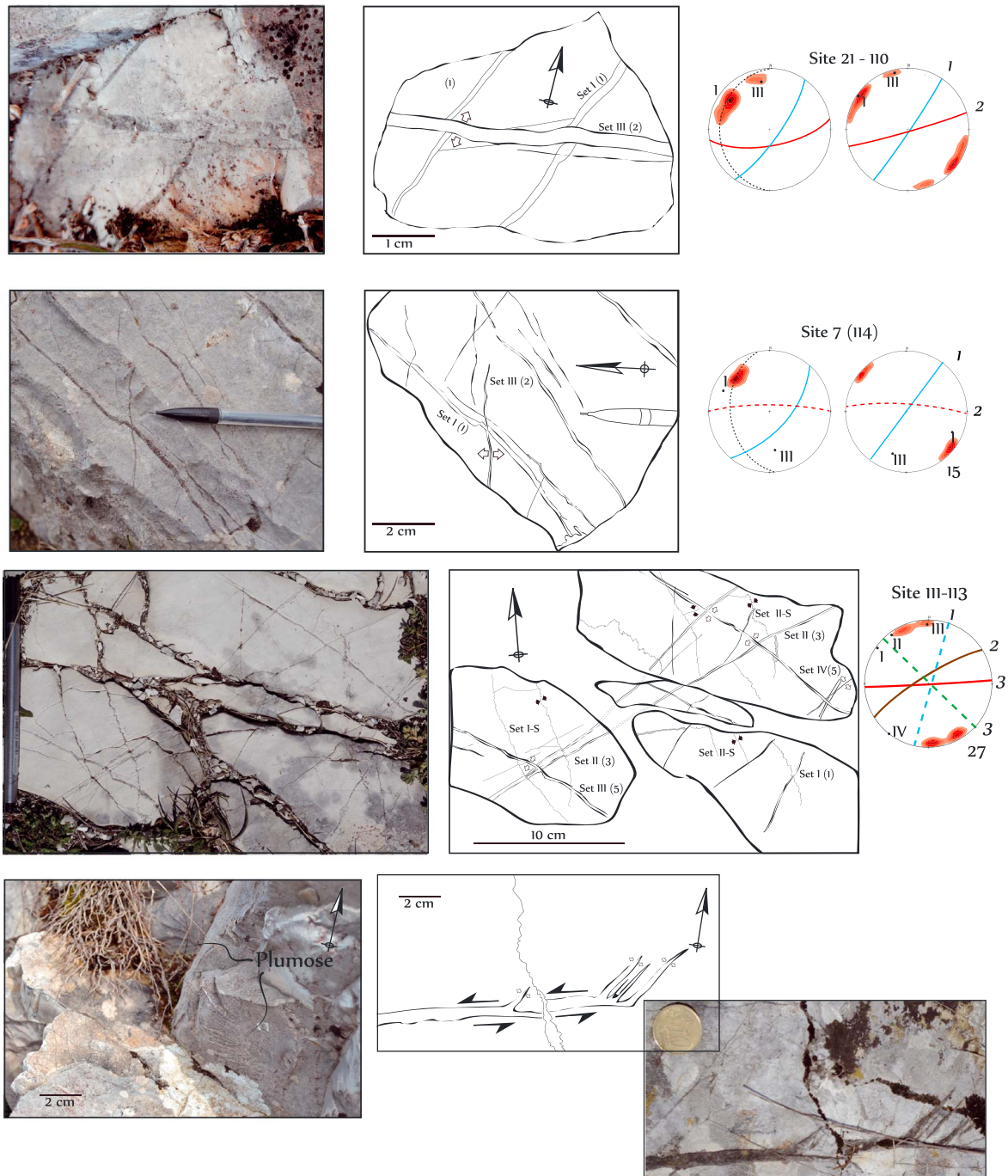


**Figure 3.** Photographs and interpretation of chronological relationships between fracture sets and microstructures as observed in the field. Corresponding data are represented as poles on Schmidt's lower hemisphere stereonet and related fracture set mean orientation are reported as planes. The current orientation of data (left stereonet) is reported once corrected using the local bed-tilting (right stereonet). Refer to Figure 5 for keys relative to stereonets.

of the Scaglia group and the limestones of the Maiolica Fm, where 700 fracture and stylolite measurements were collected with detailed mapping of chronological relationships inferred from abutment and crosscutting relationships (Figure 3). Mode I fractures (joints and veins) were treated together in this analysis in accordance with their opening mode that is supported by plumose structures (Figure 3), offset of preexisting features in the matrix or crystal growth in veins (Figure 4a) following the classification of *Bons et al.* [2012]. Mode I fracture planes and tectonic stylolite planes were plotted on Schmidt stereonet (lower hemisphere). Fracture sets were each defined by (1) a mean plane calculated statistically with a  $10^\circ$

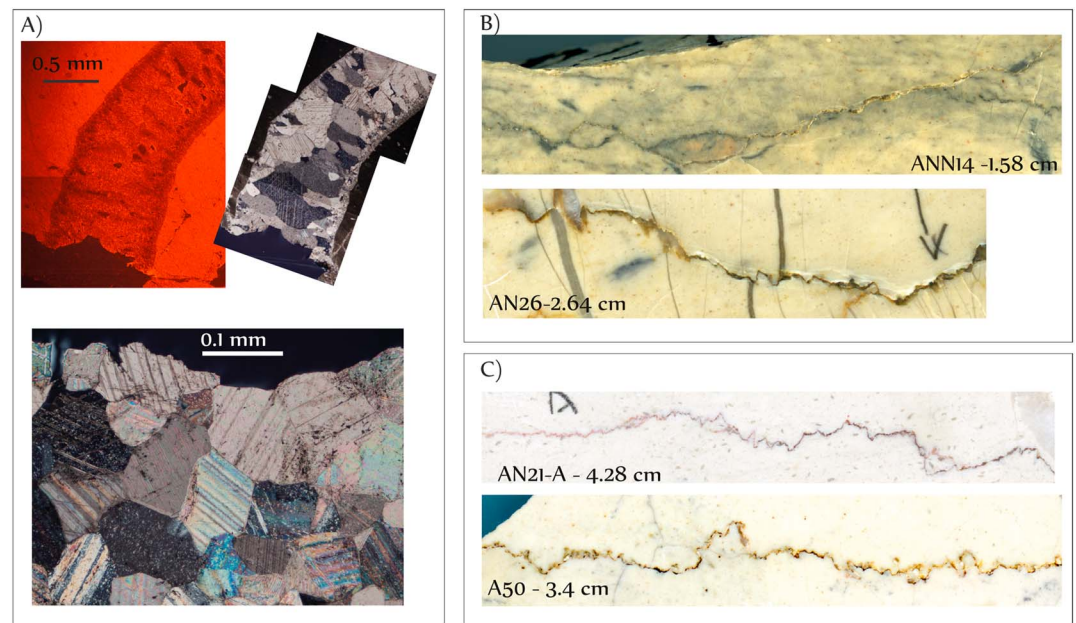


**Figure 4.** (a) Microphotographs of a syntaxial vein and corresponding observation under cathodoluminescence performed to check the diagenetic state of calcite crystals, along with details of a calcite vein that exhibits thin and dense twinning (sample A50). (b and c). Various 12,800 dpi 2-D scans of sedimentary (Figure 4) and tectonic stylolites (Figure 4c).

accuracy by the mean of a Fisher test based on the density of pole distribution (Figure 5), (2) a similar mode of deformation, and (3) consistent chronological relationships with respect to the other fracture sets or with respect to strata tilted by folding [Engelder, 1987]. The chronological relationships between fracture development and fold-related bed tilting are established on the assumption that joints and veins tend to

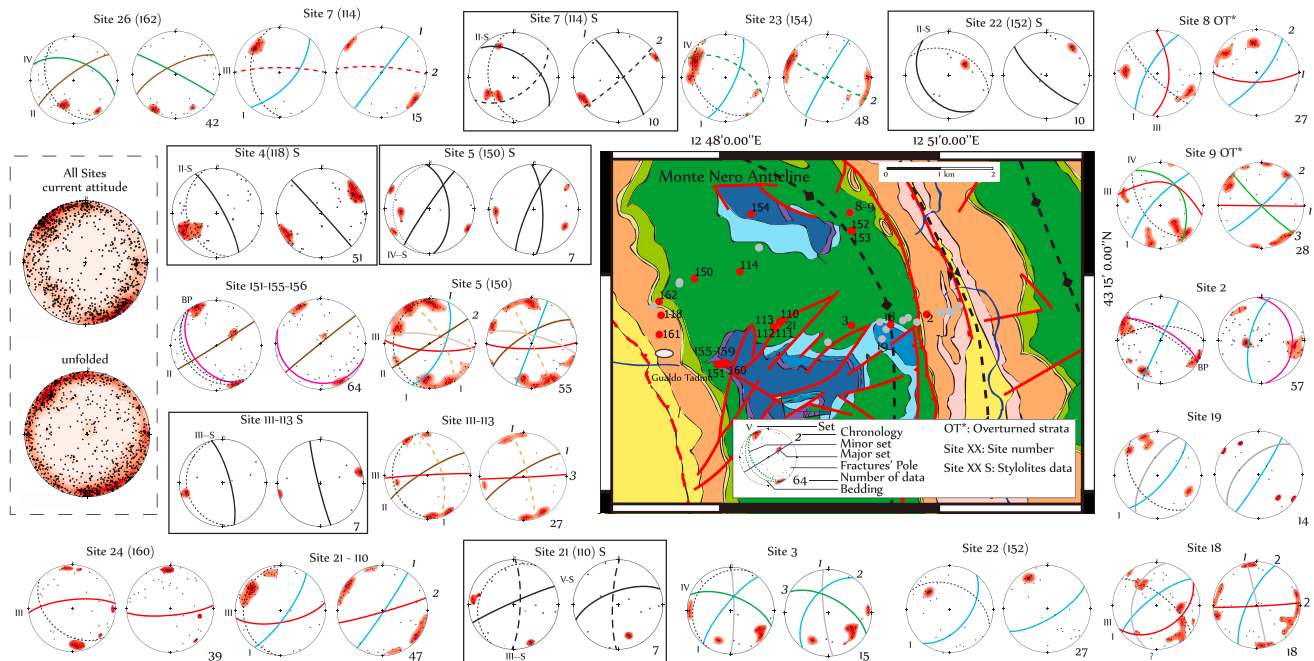


**Figure 5.** (left) Joints and stylolite orientation as measured on sites in their current orientation and (right) corrected using the local bed-tilting. The bedding planes are reported as a black short-dotted lines. The results are reported as poles on Schmidt's lower hemisphere stereonet and mean fracture set orientations are reported as planes. Yellow planes represent set I, light blue set II, brown set III, red set IV, and green set V. Those fracture sets are defined by the mean of a Fischer statistical test that defines pole density of which maximum values are reported in red.

develop under an Andersonian stress regime, i.e., with one vertical stress axis [Anderson, 1951]. A joint can be considered as opening with respect to the Anderson criterion if its dip angle is larger than  $75^\circ$  [Pollard and Aydin, 1988]. To check the pretilting chronology of objects, we correct the measured mesostructure orientation from the local strata orientation, assuming that strata were horizontal before folding with respect to observed polarity of the strata. So hereinafter the term “pretilting” refers to all objects which are interpreted as predating strata tilting during folding. Following this principle, joints and veins can be used as rough stress direction indicators as they form normal to the  $\sigma_3$  axis [Engelder, 1987]. Stylolite teeth can as well be used to reconstruct the orientation of the maximum principal stress, being parallel to the  $\sigma_1$  axis [e.g., Stockdale, 1943; Park and Schot, 1968; Petit and Mattauer, 1995], even in cases where the  $\sigma_1$  axis rotated during stylolite growth [Koehn et al., 2007].

### 3.2. Stresses From Calcite Twin Analysis

Calcite twins are common features in calcite veins and limestone host rocks (Figure 4a). In order to form, e-twinning in calcite requires that the resolved shear stress (RSS) on twin planes exceeds a critical value of  $10 \pm 4$  MPa that depends on grain size [e.g., Rowe and Rutter, 1990] and on internal twinning strain because calcite hardens once twinned [e.g., Laurent et al., 2000; Lacombe, 2010]. This critical resolved shear stress has a small dependence on temperature, strain rate, or confining pressure, which makes calcite twinning a good paleopiezometer.

The inversion process used herein is very similar to that used for fault slip data [Etchecopar, 1984], since twin gliding along the twinning direction within the twin plane is geometrically comparable to slip along a slicken-side lineation within a fault plane. It takes into account both the twinned and the untwinned planes, the latter being those of the potential e-twin planes that never experienced a RSS of sufficient magnitude to cause twinning. The inverse problem consists in finding the stress tensor that best fits the distribution of twinned and untwinned planes. The basic hypothesis is that the RSS acting on any twinned plane is higher than or at least equal to the critical RSS, while the RSS remains lower than the critical value for untwinned planes.

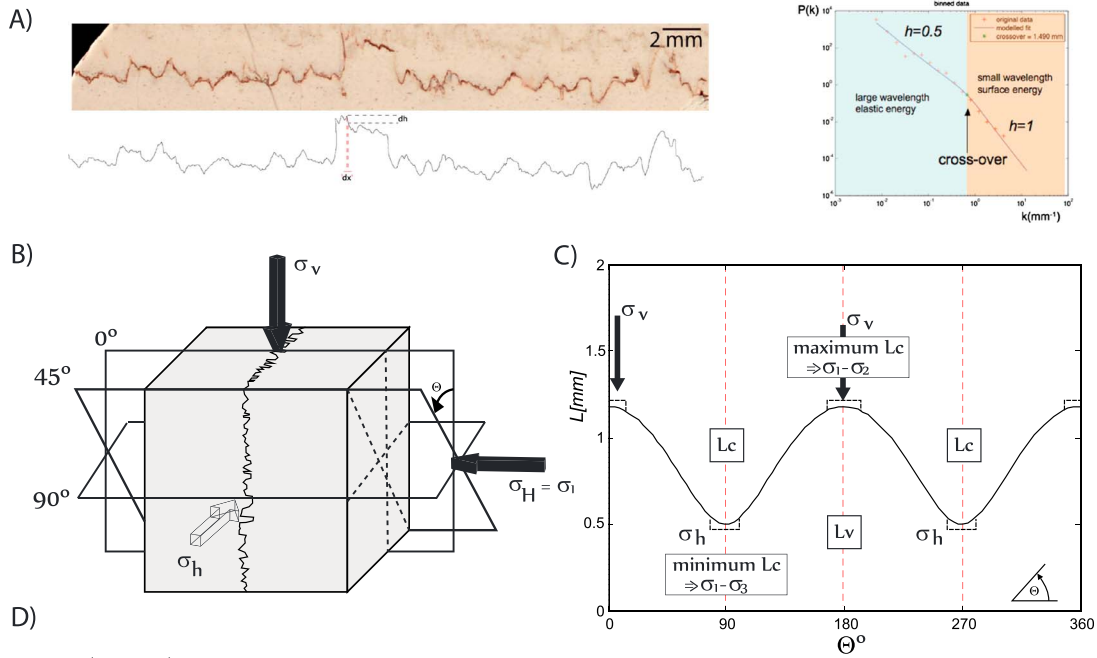
This technique yields simultaneously the orientation of the principal paleostress axes, the stress ratio  $\Phi$  ( $\Phi = (\sigma_2 - \sigma_3) / (\sigma_1 - \sigma_3)$ ) and the magnitude of the peak differential stress  $\sigma_{dmax} = \sigma_1 - \sigma_3$  (for a complete description and discussion over the method, refer to Lacombe [2007]). In cases where more than 30% twinned planes in a sample are not explained by a unique stress tensor, the inversion process is repeated with the uncorrelated twinned planes and the whole set of untwinned planes (the latter must remain untwinned irrespective of the successive stress states of the rock during its tectonic history). This procedure provides an efficient way to separate superimposed twinning events and to calculate related stress tensors where polyphase deformation has occurred. Numerous studies have demonstrated the potential of the technique to derive regionally significant stress patterns in monophase and polyphase tectonics settings [e.g., Lacombe et al., 1990, 2007; Rocher et al., 2000; Amrouch et al., 2010, and references therein].

A relative chronology between successive twinning events in vein-filling calcite and related paleostresses can be established by comparing the orientation of computed stress axes with the orientation of veins from which measurements were taken. This approach is based on the fact that a stress tensor determined from calcite grains filling a vein with a  $\sigma_3$  axis perpendicular to the vein strike is likely related to the vein formation, while other tensors with stress axes inconsistent with the vein geometry reflect later, postopening stress regimes [Lacombe, 2010]. Sampling in fold limbs also constrains the chronology of twinning relative to tilting due to folding. The orientation of the reconstructed principal stress axes with respect to strata orientation in their current attitude can help decipher whether the state of stress predates, is synchronous, or postdates strata tilting. In the cases where one principal stress axis is vertical ( $\pm 10^\circ$ ) and the two others principal stresses are in the horizontal plane, either in the current attitude of the strata or after unfolding, then the stress tensor is thought to have prevailed after or before folding, respectively. Otherwise, if for instance the maximum principal stress axis is inclined consistently less than, but in the same direction as bedding dip, then it can be considered as synfolding. The latter is true only if folding occurred under a constant stress regime and without any rotation of strata around a vertical axis.

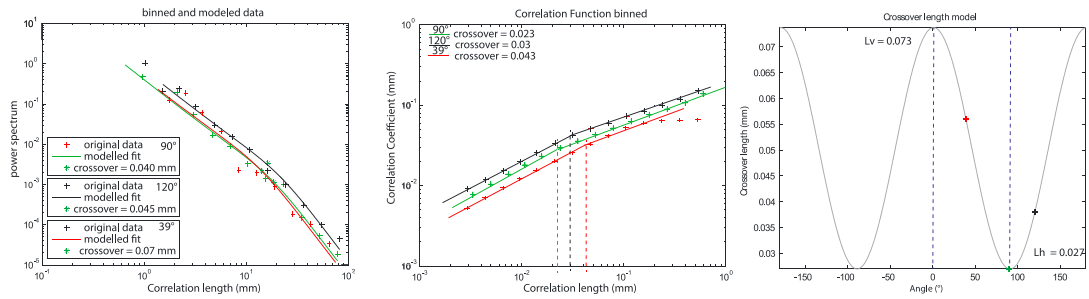
### 3.3. Stress Analysis From Stylolite Roughness

The use of stylolites in paleostress reconstruction has been limited for a long time to the correlation between teeth orientation and maximum principal stress  $\sigma_1$  [Park and Schot, 1968; Arthaud and Mattauer, 1969; Asaro

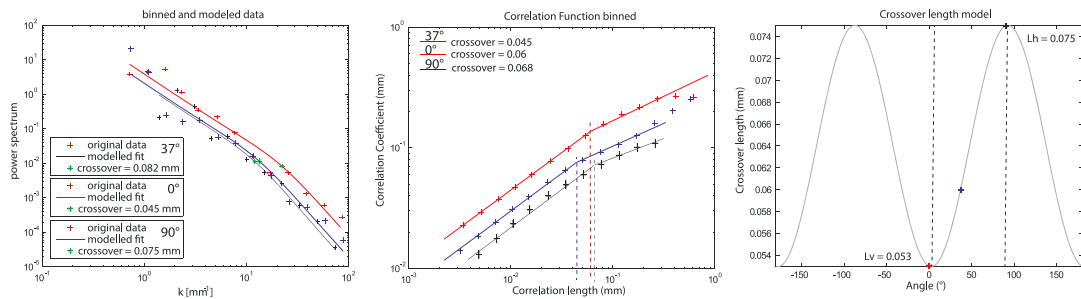




AN5 (Set II-S)



AN6 (Set IV-S)



A49 (Set IV-S)

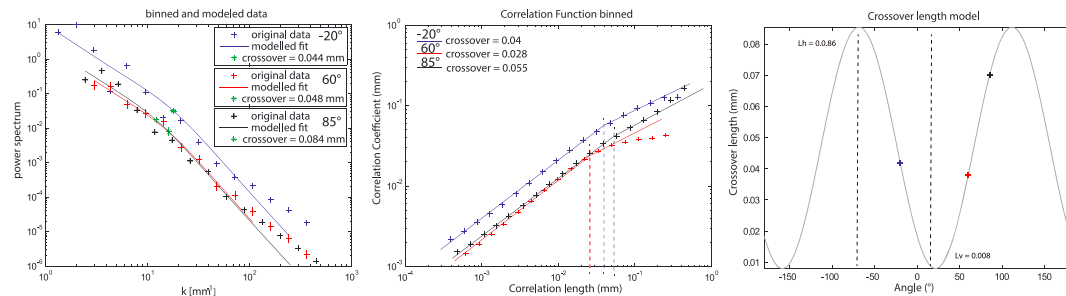


Figure 6

and Tiller, 1972; Petit and Mattauer, 1995]. Recent studies show that stylolite roughness has a self-affine scaling invariance over several orders of magnitudes [Schmittbuhl *et al.*, 2004; Renard *et al.*, 2004]. This is a result of the thermodynamics and kinetics of the growth of a stylolite [Koehn *et al.*, 2007]. Once the dissolution starts, there is a competition between two stabilizing (smoothing) forces, long-range elastic forces and local surface tension, and a destabilizing (roughening) force due to pinning particles (or other heterogeneities) on the stylolitic surface. On the one hand, the stabilizing forces tend to reduce the Helmholtz free energy of the solid, meaning that they flatten the surface by preferentially dissolving areas of local roughness. On the other hand, the destabilizing force resists dissolution in specific locations, locally increasing the free energy and producing peaks and teeth. As a consequence, a fractal analysis of the stylolite roughness is expected to return two growth regimes (reflecting elastic versus surface energy dominated regimes), each of those being characterized by a roughness exponent (so-called Hurst exponent) and separated by a crossover length ( $L_c$ ) that describes the scale at which the switch between regimes of control occurs (Figure 6a). This is clearly seen on a Log-Log plot where each regime is represented by a slope and where the  $L_c$  is the meeting point of the slopes. The link between crossover length and stress field has been established based on stylolite section and considering an isotropic stress in the stylolite plane, a hypothesis suited for bedding-parallel stylolites (BPS) that have been successfully used to estimate burial depth [Koehn *et al.*, 2007, 2012; Ebner *et al.*, 2009, 2010b]. These findings have been used to predict the applied normal-to-the-plane stress, and the two stress axes parallel to the plane, thus reconstructing the stress tensor and the principal stress magnitude according to the following analytical solution (1) linking crossover length  $L_c$  to stress magnitude [please refer to Schmittbuhl *et al.*, 2004 and to Ebner *et al.*, 2009]:

$$L_c = \frac{\gamma E}{\beta \sigma_m \sigma_d} \quad (1)$$

where  $\gamma$  is the surface energy at the solid-fluid interface,  $E$  is the Young modulus,  $\beta = \nu(1 - 2\nu)/\pi$  is a dimensionless number with  $\nu$  the Poisson ratio,  $\sigma_m$  is the mean stress and  $\sigma_d$  the differential stress.

### 3.3.1. Case of Bed-Parallel Stylolites

This analytical solution can be simplified when it is used to study isotropic horizontal pressure-solution planes (BPS). We assume for BPS that the maximum principal stress is vertical (i.e.,  $\sigma_v = \sigma_1$ ) and that both horizontal stresses ( $\sigma_h$  and  $\sigma_H$ ) are equal and smaller. Under the assumption of zero horizontal strain, one can relate the vertical to horizontal stress via  $\sigma_h = \sigma_H = \frac{\nu}{(1-\nu)} \sigma_v$  (in this paper,  $\sigma_H$  is the principal horizontal stress with the higher magnitude and  $\sigma_h$  with the smaller magnitude), and consequently  $\sigma_m \sigma_d = \alpha \sigma_v^2$  with  $\alpha = \frac{1}{3} \left( \frac{1+\nu}{1-\nu} \right) \left( \frac{1-2\nu}{1-\nu} \right)$  [Ebner *et al.*, 2009].  $L_c$  is then written as function of the vertical stress

$$L_c = \frac{\gamma E}{\beta \alpha \sigma_v^2} \quad (2)$$

and may be used to reconstruct the vertical stress hence the burial depth of the rock (at the time of stylolite activity) from the roughness of bed-parallel stylolites. In the present study, we use 2-D high-resolution scans (12,800 dpi) of hand cut slabs polished down to 5  $\mu\text{m}$  (Figures 4b and 4c). We then digitalize the stylolite by hand with a 5 pixel-pen tool and perform the inversion process under matlab as proposed by Ebner [2009]. For each inversion and considering the sensibility of the crossover length with respect to the signal analysis method, we apply a Fourier transform and a correlation function signal analysis and select the  $L_c$  that best fits the expected Hurst coefficient or determine an average when both methods give back a good fit. To limit

**Figure 6.** (a) Methodological section defining the roughness as we use it on the left-hand side and defining the Hurst exponent and Correlation length on a log-log plot of the power function of the Fourier Transform on the right-hand side. (b) Sketch showing the ideal cuts performed on a tectonic stylolite to reconstruct anisotropy and the definition of angle  $\theta$  (modified after Ebner *et al.* [2010b]). (c) Reconstructed evolution of the crossover length  $L_c$  regarding the angle  $\theta$ ,  $0^\circ$  and  $180^\circ$  being the vertical line of the stylolite plane. These evolutions were obtained from 3-D scans of open surfaces [Ebner *et al.*, 2010b]. (d) Examples of tectonic stylolite roughness inversion over three samples. Each sample has been cut along three or more planes parallel to the teeth at an angle with respect to the vertical plane containing the stylolite (which is  $0^\circ$ , angle measurements are counterclockwise). Each stylolite roughness is studied and inversion is carried out by means of a fast Fourier transform (left column) and correlation function (middle column). A sinusoid function is then computed to reflect the anisotropy of the cross-over length with respect to the angle along which the stylolite is observed (right column). Minimum and maximum crossover lengths are then inferred, which can be associated to the vertical crossover length or to the horizontal crossover length.

uncertainties due to noise, we use a median value of  $L_c$  obtained from different parallel cuts of the same stylolite, in order to check isotropy of the signal, and from different stylolite lengths on the same cut, in order to check the fractal properties. For either isotropic or anisotropic stylolites, we solve equation (1) or (2) considering a surface free energy along the solid-fluid of  $\gamma = 0.23 \text{ J/m}^3$  for calcite [Wright *et al.*, 2001] and a Poisson ratio  $\nu = 0.25 \pm 0.05$  [Clark, 1966].

In order to solve equation (1) or (2) and calculate stress, we need to consider a value for the Young modulus  $E$ . As this parameter has a strong impact on the calculated stress, and as the value for the Young Modulus is highly variable in the literature, we calculated it following the method described by Ebner *et al.* [2009]. The relative value of the principal normal (vertical) stress  $\sigma_v$  of a population of horizontal stylolites that are located at different depth is plotted as a function of  $L^{-1/2}$ . The population should define a linear trend if all stylolites formed roughly at the same time. The value of  $E$  is a function of the slope of a line through the population calculated as a function of two points on this line of coordinates  $[\sigma_{v(1,2)} - L_{c(1,2)}^{-1/2}]$  and can be derived from equation (2) for an isotropic case:

$$E = \left( \frac{\sigma_{v2} - \sigma_{v1}}{L_{c(1,2)}^{-1/2} - L_{c(1,2)}^{-1/2}} \right)^2 \alpha \frac{\beta}{\gamma} \quad (3)$$

where  $\frac{\sigma_{v2} - \sigma_{v1}}{L_{c(1,2)}^{-1/2} - L_{c(1,2)}^{-1/2}}$  is the slope of the linear trend on the plot,  $\alpha = \frac{1}{3} \frac{(1+\nu)}{(1-\nu)}$ ,  $\beta = \nu(1 - 2\nu)/\pi$ , and  $\gamma$  the surface free energy along the solid-fluid interface.

### 3.3.2. Case of Tectonic Stylolites

In order to use the anisotropic tectonic stylolites as paleopiezometer Ebner *et al.* [2010b] conducted a 3-D study of open tectonic stylolite surfaces that showed that the tectonic stylolite morphology records a stress anisotropy within the stylolite plane. Depending on the orientation of the stylolite the crossover length,  $L_c$ , reflects the differential stress  $\sigma_d$  between  $\sigma_1$  and  $\sigma_2$ ,  $\sigma_1$ , and  $\sigma_3$  or a value in-between and thus affects the crossover length, as seen from equation (1). If the crossover is only determined from a 2-D signal, then it depends on the orientation of the cut through the stylolite plane that is analyzed with respect to the principle stress orientations ( $\sigma_2$  and  $\sigma_3$ ) or a reference angle  $\theta$  [Ebner *et al.*, 2010b]. The relationship between  $L_c$  and the  $\theta$  is a periodic function, of which minimum and maximum  $L_c$  are separated by  $90^\circ$  (Figure 6b). Consequently, because open stylolite surfaces are hard to find in nature, we reconstruct the periodic function that describes the radial evolution of the  $L_c$  of the stylolite using 2-D scans of three surfaces normal to the stylolite plane, each separated by at least  $40^\circ$  in direct sense (counterclockwise),  $0^\circ$  being along the stylolite plane once put back in its initial position (Figure 6b). The inversion is then carried out as described previously for each face, at least on each of the mirror faces. The three  $L_c$  and corresponding angles  $\theta$  are filled into equation (4) to reconstruct the periodic function of the crossover length ( $L_c$ ) using the angle with respect to the vertical direction ( $\theta$ ). Because we know that the period is  $180^\circ$  given by the observation of natural open tectonic stylolites [Ebner *et al.*, 2010b] (Figure 6c):

$$L_{c(\theta)} = a + b \sin(2\theta + c) \quad (4)$$

where  $a$ ,  $b$  and  $c$  are a function of (1) the crossover lengths constructed from each face and (2) the angle  $\theta$  between the face and the vertical axis once the stylolite plane is vertical. The parameters  $a$ ,  $b$ , and  $c$  of the sinusoidal function can then be determined from the following equations (for equations (5.1) and (5.2), refer to Appendix A for the complete derivation)

$$a = L_{c1} - b \sin(2\theta_1 + c) \quad (5.1)$$

$$b = \frac{(L_{c2} - L_{c1})}{\sin(2\theta_2 + c) - \sin(2\theta_1 + c)} \quad (5.2)$$

$$c = \tan^{-1} \left( - \frac{\Delta L (\sin 2\theta_3 - \sin 2\theta_1) - (\sin 2\theta_2 - \sin 2\theta_1)}{\Delta L (\cos 2\theta_3 - \cos 2\theta_1) - (\cos 2\theta_2 - \cos 2\theta_1)} \right) \quad (5.3)$$

where  $\Delta L = \frac{L_{c2} - L_{c1}}{L_{c3} - L_{c1}}$ . The minimum and the maximum of the  $L_c$  correspond to the maximum and minimum differential stresses with respect to the main horizontal stress that formed the tectonic stylolite ( $(\sigma_1 - \sigma_3)$  and  $(\sigma_1 - \sigma_2)$ ), respectively (Figure 6bc). When the  $\theta$  associated with  $L_{c\min}$  is close to the vertical plane of the tectonic stylolite (i.e.,  $0^\circ \pm 15^\circ$ ), then the stress regime corresponds to strike-slip deformation ( $\sigma_2$  is vertical, e.g., A49 in Figure 6d); otherwise, if the  $\theta$  associated with  $L_{c\max}$  is close to  $0^\circ$ , then the stress regime is contractional ( $\sigma_3$  is vertical, e.g., AN6 in Figure 6d). In some cases, the  $\theta$  associated with  $L_{c\min}$  and  $L_{c\max}$

cannot be considered as being aligned with respect to the main principal stresses, which probably means that they developed under a non-Andersonian stress regime. In those cases,  $L_v$  and  $L_h$  are not related to  $L_{cmin}$  and  $L_{cmax}$ , and so inversion to principal stress is not possible. For the sake of simplicity, we will refer to strike-slip related stress regimes to describe the state of stress where  $\sigma_2$  is vertical, according to Anderson.

After the reconstruction of the anisotropy effect on  $L_c$ , we solve the following equation to access the stress magnitude for the horizontal and vertical stresses (the reader is referred to *Ebner et al.* [2010b] for a complete description):

$$\frac{L_h}{L_v} = \frac{\sigma_H - \sigma_v}{\sigma_H - \sigma_h} \quad (6)$$

where  $L_h$  and  $L_v$  are the crossover length maxima in the horizontal orientation and in the vertical orientation of the plane of the stylolite, respectively, and where  $\sigma_H$  and  $\sigma_h$  are the values of the maximum and minimum horizontal principal stresses, and  $\sigma_v$  the magnitude of the vertical principal stress. An independent estimate of  $\sigma_v$  is required to obtain the values of  $\sigma_H$  and  $\sigma_h$  by solving the following equations derived from equation (6) (please refer to Appendix A (part of *Ebner et al.* [2010b]) for the complete derivation):

$$\sigma_h = \sigma_H - \frac{L_v}{L_h}(\sigma_H - \sigma_v) \quad (7)$$

$$\sigma_H^2 + \sigma_H \frac{2\sigma_v \left(\frac{L_v}{L_h}\right)^2 - \sigma_v \frac{L_v}{L_h} - \sigma_v^2 \frac{L_v}{L_h} - \sigma_v^2 \left(\frac{L_v}{L_h}\right)^2 - 3\frac{A}{L_h}}{2\frac{L_v}{L_h} - \left(\frac{L_v}{L_h}\right)^2} - \frac{\sigma_v^2 \frac{L_v}{L_h} - \sigma_v^2 \left(\frac{L_v}{L_h}\right)^2}{2\frac{L_v}{L_h} - \left(\frac{L_v}{L_h}\right)^2} = 0 \quad (8)$$

where  $A = \gamma E / \beta$ . Because the solution of equation (8) is a binomial formula, each inversion gives back two distinct solutions for  $\sigma_H$  and  $\sigma_h$ . A previous analysis found that one of these two solutions is typically impossible, i.e., negative [*Ebner et al.*, 2010b].

To obtain reliable values of stress magnitudes, we considered only some stylolites regarding their amplitude and wavelength, because a high amplitude of teeth is likely related to strong pinning effects, which can disturb the inversion process [*Koehn et al.*, 2007]. According to the classification of *Park and Schot* [1968], we did not consider any stylolite falling in one of the following classes: rectangular up and down, seismograph, and smooth stylolites. This selection minimizes the nonnegligible uncertainties that arise as a function of the stylolite morphologies [*Rolland et al.*, 2014] mentioned in the introduction.

## 4. Results

### 4.1. The Sequence of Development of Fracture and Stylolite Sets

The statistical treatment of meso-structure trends combined with their relative chronology resulted in the identification of eight sets (four joint/vein sets and two tectonic stylolite sets: Figure 3), which are documented at the scale of the MNA (Figure 5). No specific stratigraphic control over the distribution of fracture sets was observed. The oldest microstructure set (I) comprises bed-perpendicular N020 striking joints and veins (orientation after unfolding). The bed-perpendicular N050 (orientation after unfolding) joints and veins of the set II abut or crosscut microstructures from set I. Sets I and II are the most widely encountered over the fold, and numerous stylolites fall into the set II-S, showing N050-oriented teeth and bed-perpendicular N140-striking planes. Set III comprises bed-perpendicular fractures and veins striking N090–N110. This set III is found in all fold positions, and the related fractures and veins abut or crosscut veins and fractures from sets I and II. In the overturned bed of the forelimb, however, the chronology is reversed, and N090-striking veins are bed-perpendicular and seem to predate N020 striking veins. Some N090 veins exhibit horsetail terminations that suggest a later reactivation under a left-lateral shear (Figure 3). We document a related set of tectonic stylolites with teeth oriented N090 and planes striking N180. The last set, set IV, comprises bed-perpendicular N135 striking veins, which are rarely encountered at fold scale and are observed near the NNW-SSE striking hinge and in some locally curved strata in the backlimb. The joints and veins of set IV crosscut or stop onto joints and veins from sets I and II. Few direct chronological relationships are observed with set III, so it was not possible to establish a sequence between these two sets from field observations.



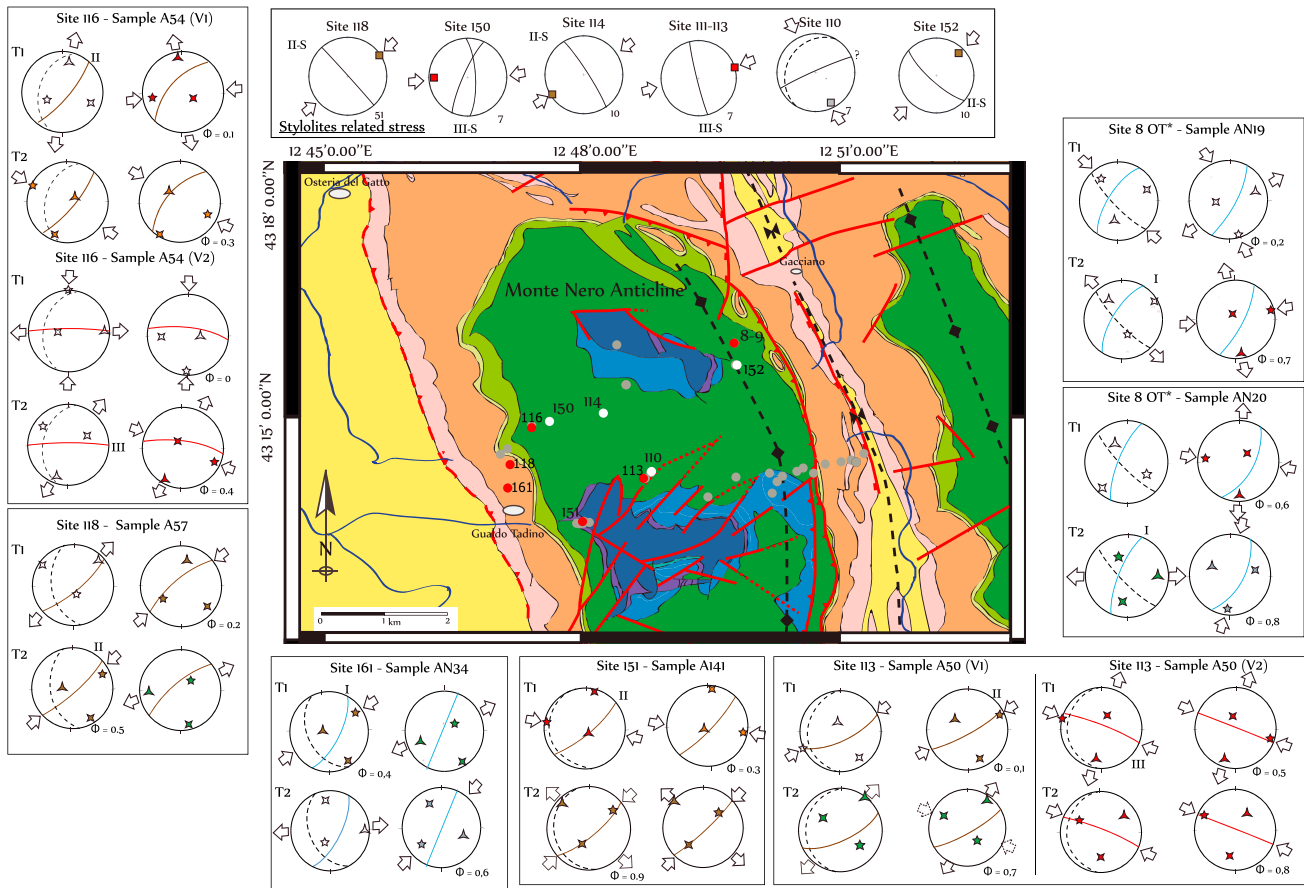


**Figure 7.** Paleostress orientations inferred from stylolite orientation sets and paleostress orientations reconstructed from calcite twinning (Schmidt's stereonets). Square represents  $\sigma_1$  inferred from stylolite sets, five-branch star represents  $\sigma_1$ , four-branch star represents  $\sigma_2$ , and three-branch star represents  $\sigma_3$ . Colors in stars follow the same key than fracture sets on Figure 3. The fracture set from which the stress tensor is reconstructed is reported on the stereonet as roman number. The folded/unfolded attitude is reported for each case from the left to the right. The solid arrows indicate directions of compression/extension; the dotted arrows represent alternative interpretation according to stress axis permutation when the stress ratio ( $\phi$ ) is close to 0 or 1.

### 4.2. Paleostress Orientations and Magnitudes From Calcite Twins

Calcite twin inversion was carried out in different sedimentary formations covering all structural positions over six sampling sites. Seventeen stress tensors were reconstructed from twinned calcite in veins belonging to the identified fracture sets (Figure 7 and Table 1). Calcite grains were deformed in a thin-twin strain regime, suggesting that temperature did not exceed 170–200°C [Ferrill *et al.*, 2004] (Figure 4a). Twinning strain is below 3–4%; this internal strain was considered along with the mean grain size to define the critical RSS used for the calculation of the differential stress [Rocher *et al.*, 2004; Amrouch *et al.*, 2010], as reported in Table 1. In some cases, the computed ratio  $\phi$  is close to 0 or 1, indicating possible stress permutations. When the ratio  $\phi$  is 0.1 or 0.9, one can consider both stress regimes to be equally reliable with respect to permutation  $\sigma_2 \leftrightarrow \sigma_3$  or  $\sigma_1 \leftrightarrow \sigma_2$ , respectively (e.g., site 113-A50 V1-T1; Figure 7 and Table 1). For the sake of clarity, all examples reported in the following part are shown in Figure 7 and Table 1, where T1 and T2 correspond to first and second tensors given by the inversion process, irrespective of their actual relative chronology.

A pretilting compressional stress tensor with  $\sigma_1$  trending N020 reconstructed in a vein from set I (striking N020, site 8OT, sample AN20-T2); another pretilting compressional stress with  $\sigma_1$  trending N040–N060 is reconstructed in the backlimb of the fold from veins from set I (site 161, AN34-T2) and set II (site 113, A50V1-T1 and site 118, A57-T1). Additionally, a strike-slip compatible stress tensor with  $\sigma_1$  striking N040–N060 consistent with opening of the veins of set II is recognized in site 151 (sample A141-T2). These stress tensors that are related to sets I and II exhibit a maximum differential stress  $\sigma_{dmax}$  ranging from 26 to 106 MPa, with a mean value of about 60 MPa. A later pretilting event is illustrated by one compressional stress tensor with  $\sigma_1$  striking

**Table 1.** Paleostress Tensors Calculated From Inversion of Calcite Twin Data<sup>a,b</sup>

Sample	GPS	Formation	Bedding Strike-Dip	Vein Strike-Dip	Tensor	Trend (plunge) of the Principal Stress Axes (degree)			$\sigma_3$	$\phi$	Mean Crystal Size ( $\mu\text{m}$ )	Total Number of Data (T/UT)	Number of Consistent Data (T/UT)	CRSS (MPa)	$\sigma_1 - \sigma_3$ (MPa)
						$\sigma_1$	$\sigma_2$	$\sigma_3$							
A50	113	Maiolica	6 19W	65 70* 79S*	T1	238 (6)	147 (17)	347 (72)	0.1	300 ± 70	168/72	84/69	10	106 ± 10	
					T2	68* (9)	154* (29)	318* (63)	0.7		84/72	39/62	40 ± 4		
A54	116	Maiolica	15 42W	111 84N 112* 89N*	T1	285 (7)	29 (6)	191 (25)	0.5	400 ± 90	173/61	89/58	10	52 ± 5	
					T2	105* (12)	348* (65)	199* (22)	0.8	90/61	41/57	50 ± 5			
A57	118	Scaglia Rossa	170 45W	44 77E 42* 66W*	T1	246 (5)	116 (2)	14 (2)	0.1	600 ± 110	147/51	76/49	7	56 ± 2	
					T2	262* (17)	129* (6)	358* (17)	0.3	83/51	37/43	40 ± 5			
A141	151	Massiccio	165 18W	90 85N 97* 76N*	T1	3 (3)	262 (7)	94 (1)	0.0	600 ± 90	122/52	47/50	7	65 ± 5	
					T2	184* (6)	278* (3)	86* (5)	0.4	77/52	28/45	30 ± 2			
AN19	80T	Maiolica	136 79SW	50* 75N*	T1	164 (7)	304 (1)	36 (1)	0.2	630 ± 160	153/60	64/57	7	60 ± 10	
					T2	237* (4)	126* (2)	19* (3)	0.5	89/60	34/52	33 ± 4			
AN20	80T	Maiolica	136 79SW	28 21* 69W 70E*	T1	48* (6)	168* (1)	265* (2)	0.2	430 ± 70	91/35	40/29	8	64 ± 5	
					T2	106* (9)	14* (1)	228* (7)	0.9	51/35	22/30	26			
AN34	161	Scaglia Rossa	152 42W	27 69E 22* 85E*	T1	53 (2)	204 (5)	315 (1)	0.2	580 ± 120	223/80	93/69	7	50 ± 5	
					T2	47* (4)	219* (4)	313* (0)	0.7	129/80	47/69	51			
AN19	80T	Maiolica	136 79SW	22 34* 74W 60E*	T1	323 (2)	68 (2)	193 (5)	0.6	400 ± 80	79/38	28/32	8	31	
					T2	162* (1)	267* (6)	68* (2)	0.8	51/38	21/36	64			
AN34	161	Scaglia Rossa	152 42W	27 22* 69E 85E*	T1	79* (5)	326* (7)	171* (1)	0.4	400 ± 100	119/58	52/52	9	78	
					T2	182* (1)	78* (2)	298* (5)	0.6	68/58	28/58	35			

<sup>a</sup>Notes: Orientations of bedding reported in italic refer to overturned strata; principal stress orientations reported with an asterisk are corrected for bed tilting.

<sup>b</sup>CRSS: Critical resolved shear stress depends on grain size and internal twinning strain; T/UT: twinned/untwinned plane.

**Table 2.** Results From Sedimentary Stylolite Roughness Inversion<sup>a</sup>

Sample	GPS	Formation	Structure	$L_c^b$ (mm)	$\sigma_v$ (MPa)	depth (km)
AN3	2	Scaglia Rossa	Forelimb	0.04	95	4.0
				0.076	69	2.9
				0.071	71	3.0
AN26	2	Scaglia Rossa	Forelimb	0.095	61	2.6
				0.086	65	2.7
				0.089	63	2.7
AN24	10	Scaglia Rossa	Forelimb	0.12	54	2.3
AN35	161	Scaglia Rossa	Backlimb	0.035	101	4.3
AN16	114	Maiolica	Backlimb	0.088	64	2.7
AN15	115	Maiolica	Backlimb	0.075	69	2.9
AN14	150	Maiolica	Backlimb	0.050	85	3.6

<sup>a</sup>All depths are calculated considering a mean density of 2400 kg/m<sup>3</sup>.  
<sup>b</sup>Average crossover length computed from several measurements, see text for details.

N110 characterized by a  $\sigma_{dmax}$  of 50 MPa (site 113, A50V2-T2) and by four strike-slip compatible stress tensors with  $\sigma_1$  striking N080–N100 (site 8OT, AN19-T2/AN20-T1 and site 116, A54V1-T1/V2-T2). The reconstructed  $\sigma_{dmax}$  is similar for all these tensors, ranging from 30 to 56 MPa, with a mean value of around 50 MPa. This event is observed regardless of formation or structural position and is reconstructed from calcite veins from sets I, II, and III. Another pretilting event postdating the set III consists of a compressional/strike-slip (close to permutation) compatible stress tensor with  $\sigma_1$  striking N180 (site 116, A54V2-T1), with a  $\sigma_{dmax}$  value of 65 MPa.

An extensional stress tensor with a horizontal minimal stress ( $\sigma_3$ ) striking N045 is documented from calcite veins belonging to set II in the backlimb of the MNA (site 113, A50V1-T2) with a corresponding  $\sigma_{dmax}$  of 40 MPa. This stress tensor being characterized by a horizontal minimal stress ( $\sigma_3$ ) lying in the strata and striking perpendicular to the fold axis, either before or after strata folding, we interpret them as showing the synfolding, curvature-related extensional stress in the fold.

Two posttilting stress tensors are interpreted from inversion, without additional constraint on their relative chronology. A posttilting stress tensor with  $\sigma_1$  striking N100–N120 is recorded with one strike-slip (site 113, A50V2-T1) and one compressional (site 151, A141-T1 and site 116, A54V1-T2) regime and a reconstructed  $\sigma_{dmax}$  of 52 MPa and 40 to 64 MPa, respectively. Another posttilting event consists in a compressional stress tensor with  $\sigma_1$  striking N045 (site 161, AN34-T1 and site 118, A57-T2) characterized by a  $\sigma_{dmax}$  ranging from 33 MPa to 78 MPa. Even if the pretilting interpretation of the latter tensors seems correct, the fact that  $\sigma_1$  is horizontal in the current strata position and not normal to bedding supports a posttilting interpretation of those tensors.

From calcite twin analysis alone there is no evidence of a relative chronology between the stress field with  $\sigma_1$  striking N100 and the stress field with  $\sigma_1$  striking N135. Nevertheless, they all are recorded in veins of set II and consequently postdate the development of set II.

### 4.3. Maximum Burial Depth From Bedding-Parallel Stylolites (BPS)

We performed a roughness analysis on eleven BPS in the Maiolica Fm and in the Scaglia Rossa Fm., in both the backlimb and the forelimb of the MNA and in the syncline located east of the MNA's forelimb (Figure 1 and Table 2). Average crossover lengths and corresponding estimated vertical stress from equation (2) are reported in Table 2, along with the calculated depth. In order to calculate the paleo-depth of the formation we used a mean density of 2400 kg/m<sup>3</sup> for the overlying rocks, which was obtained by integrating the density of each formation up to Marnoso-Arenacea Fm. (time at which folding likely occurred [Barchi et al., 2012]) using *P* wave velocities [Mirabella et al., 2008]. This value of 2400 kg/m<sup>3</sup> was used along with a surface free energy along the solid-fluid interface of  $\gamma = 0.23 \text{ J/m}^3$  for calcite [Wright et al., 2001] and a Poisson ratio  $\nu = 0.25$  [Clark, 1966]. We calculated *E* by applying the method described by Ebner [2009, part 2c of the present paper] for the Maiolica and Scaglia Rossa formations using the stratigraphic position of each sample for which we have a  $L_c$ . The top of the Scaglia Rossa formation was used as the surface for our relative depth measurements (Figure 8). The plot of  $\sigma_{v(\text{relative})} = f(L_c^{-1/2})$  successfully reconstructs the linear trend as shown by Ebner et al. [2009] with a correlation coefficient of 0.778 (Figure 8). We used this plot to solve equation (3) and obtained a value for  $E = 23.2 \text{ GPa}$  that we used for the whole stylolite inversion process.

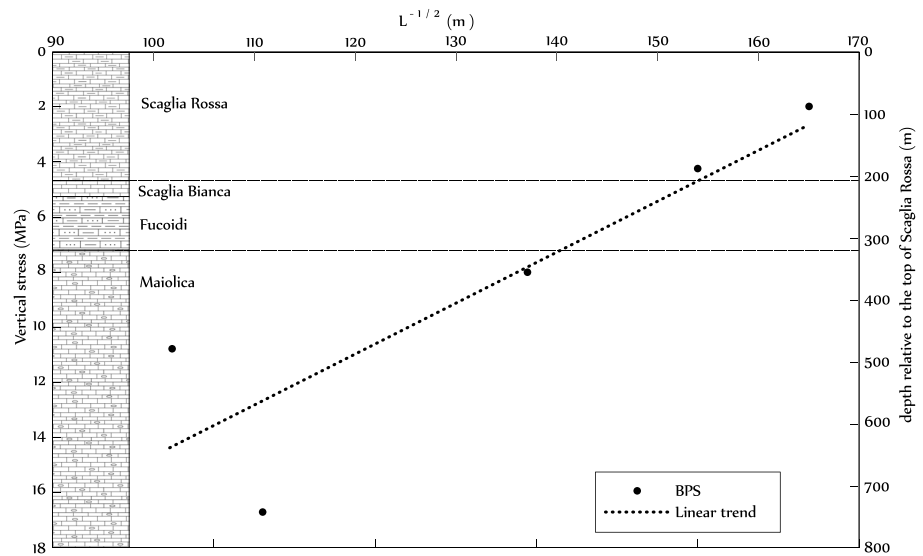


**Figure 8.** Plot of relative values of the principal normal stress as a function of  $L^{-1/2}$ . The blue dots represent values from samples of the Maiolica and Scaglia Rossa formations in the backlimb and the hinge of the MNA. The linear trend linking these points is controlled by the value of the mechanical and chemical parameters of the rocks. As there are few variations over the surface free energy  $\gamma$  or onto the poisson ratio  $\mu$ , then we can relate the slope of the trend to the young Modulus  $E$ , following the equation (3) described in the text. The trend of the stylolite population also underpins that the estimated burial depths are realistic.

The estimates of stratigraphic column thickness for the position of the base of the Maiolica Fm. range from 1220 m to 3400 m and the base of the Scaglia group from 820 to 2900 m [Jacobacci, 1979; Tavani et al., 2008]. This observed variation between estimates is related to the fact that thickness observations done on the field or in boreholes are highly sensitive to lateral differential deposition or erosion, leading to local sedimentary wedges, especially in deformed fold-thrust belts with complex polyphase history [Caricchi et al., 2015a]. From the inversion process, we reconstructed a maximum depth of the Scaglia group ranging from 2300 to 4300 m, with most of the stylolites showing a depth of 2700 m. In the Maiolica, the depth of burial ranges from 2700 to 3600 m. Variations in surface free energy and Poisson ratio have a limited to negligible impact on the reconstructed stress. Considering an uncertainty of 10% for each of these parameters leads to an uncertainty of 7% of the resulting stress value. The depth calculation from the stress is dependent on (1) the density of overburden and (2) on the assumption that the stress is isotropic in the horizontal plane, which is debatable at depth in a complex tectonic context.

#### 4.4. Tectonic Stress Magnitudes From Tectonic Stylolites

The orientations of  $\sigma_1$  inferred from the stylolite sets are reported on Figure 7. We document two main events: (1) a prefolding  $\sigma_1$  striking N050 in all the structural positions of the fold (sites 118, 114, and 152, once corrected from folding) and (2) a prefolding /postfolding  $\sigma_1$  striking N090 in the backlimb of the fold (sites 150 and 111–113). At the local scale, a postfolding  $\sigma_1$  striking N160 in the backlimb (site 110, in the current strata attitude) is also documented. This stress is likely resulting from a local heterogeneity and consequently will not be considered further as reflecting a major tectonic event.

In order to invert tectonic stylolite roughness for stress, the 3-D geometry of the crossover length  $L_c$  must be reconstructed across the stylolite plane (Figure 6d). Eleven tectonic stylolites were selected covering all the structural positions in the fold and coming from the Maiolica Fm. and the Scaglia group (Table 3). For each stylolite, three surfaces normal to the stylolite plane were digitized and  $L_c$  was computed from the frequency analysis (Figure 6d). The three different values for  $L_c$  are then used in equation (3) to construct a sinus function linking the angle of orientation of the reconstructed roughness line on the stylolite surface to the crossover length (Figure 6d). The stress regime is then deduced from the angle at which minimum and maximum values for  $L_c$  are observed (Figure 6d). In order to solve equation (5.1) linking  $L_c$  to stress, we need to fix  $\sigma_v$  [Ebner et al., 2010b] (Figure 6). As selected tectonic stylolites are likely to have developed before folding



**Table 3.** Results From Tectonic Stylolite Stress Inversion<sup>a,b</sup>

Sample	Stylolite	GPS	Formation	Structure	$L_c$ max (mm)	$L_c$ min (min)	depth (km)	$\sigma_1 - \sigma_3$ (MPa)	$\sigma_1$ (MPa)	$\sigma_2$ (MPa)	$\sigma_3$ (MPa)	$\phi$	Regime
AN21-A	Set V-S	8	Maliolica	Hinge	0.062	<b>0.017</b>	4	97	121	95	24	0.73	strike-slip
AN21-B	Set V-S	8	Maliolica	Hinge	0.147	<b>0.024</b>	4	70	106	95	36	0.84	strike-slip
AN21-C	Set V-S	8	Maliolica	Hinge	0.027	<b>0.0076</b>	5.5	157	181	129	24	0.67	strike-slip
AN25-A	Set II-S	1	Scaglia Rossa	Forelimb	<b>0.023</b>	0.023	2.7	66	130	64	64	0.00	isotropic
AN25-B	Set II-S	1	Scaglia Rossa	Forelimb	<b>0.027</b>	0.001	2.7	405	469	454	64	0.96	compressive
A50	Set II-S	113	Maliolica	Backlimb	<b>0.094</b>	0.042	2.7	37	101	84	64	0.54	compressive
AN36	Set II-S	162	Scaglia Bianca	Backlimb	0.006	<b>0.017</b>	3.6	148	222	85	74	0.07	compressive
AN5	Set I-S	118	Scaglia Rossa	Backlimb	0.073	<b>0.027</b>	3	77	99	70	22	0.62	strike-slip
AN6	Set III-S	118	Scaglia Rossa	Backlimb	<b>0.075</b>	0.053	2.7	33	96	73	63	0.30	compressive
AN18	Set III-S	114	Maliolica	Backlimb	<b>0.037</b>	0.037	2.7	46	109	63	63	0.00	isotropic
A49	Set III-S	112	Maliolica	Backlimb	<b>0.086</b>	0.008	2.7	120	183	171	63	0.90	compressive

<sup>a</sup>Notes: bold values for  $L_c$  min and  $L_{cmax}$  belong to the horizontal plane. Values reported in italic are calculated from a  $L_c$  value inferior to  $10^{-2}$  mm and likely reflect method limitation.

<sup>b</sup>Young modulus  $E$  is 34.2 GPa, Poisson ratio is 0.25 and the surface free energy  $\nu$  is 0.23 J/m<sup>2</sup>.

because they are bed-perpendicular, we consider the  $\sigma_v$  given by the local BPS, assuming that LPS-related tectonic stylolites developed at the maximum prefolding depth revealed by BPS. In addition, those depths are mainly consistent with the maximum reconstructed depth based on the sedimentary column thickness (Figure 1b) considering the timing of deformation of the MNA as a part of the innermost units of the UMAR, which is thought to have occurred during Tortonian times [Barchi *et al.*, 2012]. The calculated stress results are reported in Table 3. In accordance with BPS roughness inversion, the uncertainty is related to mechanical parameters of the rock, mainly the Young modulus, which has a strong impact on the reconstructed stress. This parameter was determined from a population of sedimentary stylolites. Uncertainties on the Poisson ratio, surface free energy, and uncertainties on  $L_{cmin}$  and  $L_{cmax}$  from function fitting have all a small effect on the reconstructed stress (8% of uncertainty on stress for 10% uncertainty on each of these parameters together).

Nine tectonic stylolites out of 11 show a successful reconstruction of an anisotropic signal by solving equation (4) using a minimum of three cuts perpendicular to the stylolite plane (Figure 6 and Table 3). The two remaining stylolites returned the same  $L_c$  on orthogonal planes, suggesting an isotropic signal, and have been inverted using equation (2) to predict  $\sigma_1$  only [Rolland *et al.*, 2014].

In the backlimb of the anticline, five anisotropic tectonic stylolites related to both prefolding and early-folding LPS (set I-S, II-S, and III-S) yield either strike-slip compatible or compressional stress regimes, with a  $\sigma_{dmax}$  ranging from 33 to 148 MPa, and a maximum principal horizontal stress  $\sigma_H = \sigma_1$  ranging from 96 to 222 MPa. In the forelimb, one anisotropic stylolite of prefolding LPS set II-S reveals a compressional stress regime, close to stress permutation, with a  $\sigma_{dmax}$  value of 405 MPa and a  $\sigma_1$  value of 469 MPa. In the overturned strata near the hinge of the fold, three stylolites interpreted as belonging to early-folding LPS set III-S yield a strike-slip compatible stress regime, with a  $\sigma_{dmax}$  ranging from 70 to 157 MPa and  $\sigma_1$  ranging from 106 to 181 MPa. The inversion of the latter can be correctly done only at a minimum depth of 4 km; otherwise, it is not possible to obtain a positive result for horizontal stresses solving equation (8). This depth of 4 km is then fixed by the equation but is consistent with the maximum depth recorded locally by the BPS (4 km in the overturned strata).

## 5. Interpretation of Results and Discussion

### 5.1. Evolution of Burial Depth During Folding

This study reports quantitative estimates of tectonic paleostress magnitudes in folded strata and associated burial depths, therefore complementing earlier works that combined calcite twinning paleopiezometry with fracture analysis and rock mechanics tests to derive paleostress magnitudes in folds [Lacombe *et al.*, 1996; Lacombe, 2001; Amrouch *et al.*, 2011]. The burial depth reconstructed from deep bedding-parallel stylolites must be considered as the maximum depth at which the dissolution was active on the stylolite planes [Koehn *et al.*, 2007; Ebner *et al.*, 2009, 2010b]. Most of the reconstructed values are roughly consistent with the maximum thickness of the overlying sedimentary column as predicted by log and outcrop studies

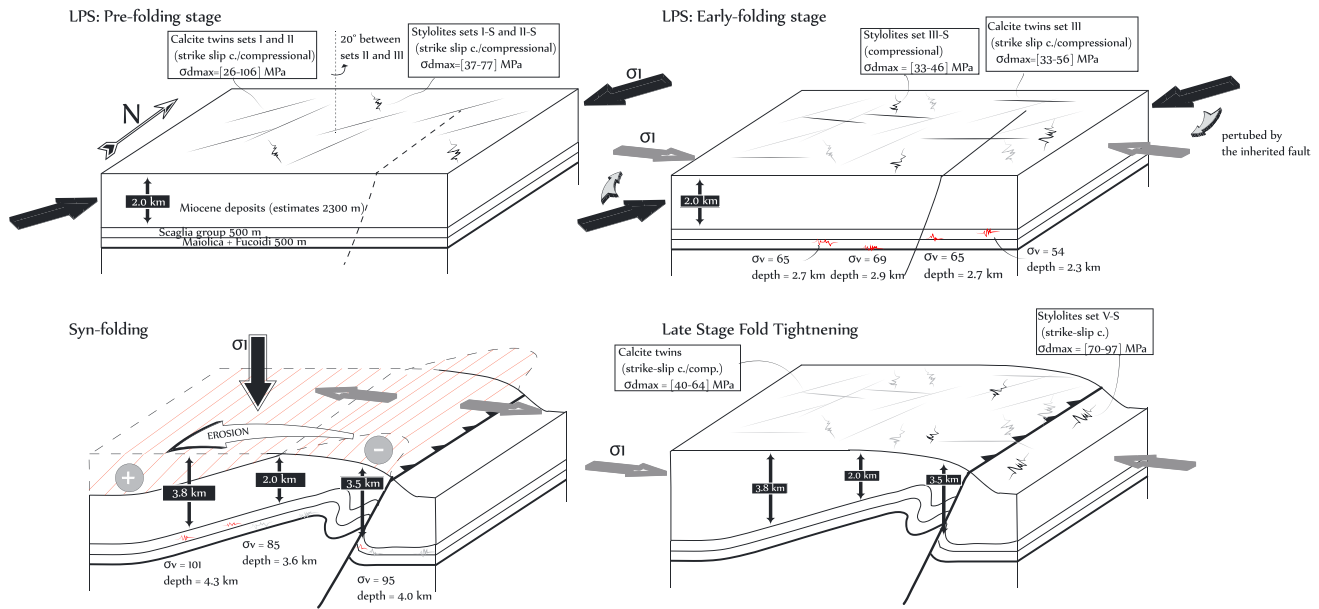


**Figure 9.** Interpretative sketch reporting the evolution of microstructure development, maximum burial evolution and stress history in the Monte Nero Anticline inferred from the whole data set including the stylolite roughness paleopiezometry. Note that only prefolding LPS and fold-related stages are represented. Drawing does not reflect microstructure distribution, abundance, or size.

(Table 2 and Figure 1b), but systematically deeper than this prediction by a few hundred meters. Even with uncertainties of 100–200 m, this consistently deeper burial indicates that thickness reconstructions based on boreholes and outcrops underestimate the maximum burial depth. The mean burial value of 2700 m derived from our results is consistent with the maximal burial depth reconstructed from vitrinite reflectance and clay content on equivalent strata in the pre-UMAR region [Caricchi *et al.*, 2015a, 2015b]. This burial depth implies deposition of 2000 m of Miocene strata before folding occurred. This thickness of the Miocene formations is documented in the UMAR, both in the innermost western part [e.g., Tavani *et al.*, 2008] and in the outermost eastern part [e.g., Petracchini *et al.*, 2012]. In the eastern part of the pre-UMAR, vitrinite reflectance and clay content also predict deeper burial (up to 4000 m), which was related to thrusting of the Ligurian units above the observed strata [Caricchi *et al.*, 2015a, 2015b]. Our data set also contains some comparable values (3600, 4000, and 4300 m; Table 2). Because (1) we are confident with the data selection and treatment, (2) the excess depth cannot be related to uncertainties, and (3) Caricchi *et al.* [2015a] showed that the Ligurian units never reached the UMAR, we propose that those values are meaningful and reflect a local burial of the strata (Figure 9) rather than a regional stacking of tectonic units. We record a 4 km depth in the overturned strata of the forelimb, and the same depth is suggested by inversion of the tectonic stylolite roughness in the overturned strata near the hinge, where we expect an average burial of 2700 m. This excess of 1300 m thickness can be explained by the geometry of the fold that leads to local increase of the thickness of overturned formations. In the backlimb we record an anomalous depth (3600 to 4300 m) west of the structural high that is formed by the hinge of the fold. We propose that the 900 to 1600 m excess overburden (considering a normal burden of 2700 m) reflects synfolding deposition of sedimentary material eroded from the hinge (Figure 9). This hypothesis is supported by the occurrence of tectonic stylolites that indicate a folding-compatible orientation of  $\sigma_1$  (N090, sample AN21; Table 3) and for which roughness inversion in terms of stress is mathematical meaningful only if we consider a burial depth of at least 4000 m. The latter stylolites then developed after synfolding extension and coeval to local burial (samples AN21-A/-B; Table 3) and can be interpreted to represent late-stage fold tightening (LSFT), as do calcite twin stress tensors of sites 113 (A50V2-T1), 151 (A141-T1), and 116 (A54V1-T1). The interpretation of both tectonic and bed-parallel stylolites is highly consistent regarding the local burial evolution and appears complementary with the more traditional analysis of fractures, allowing in the present case to define a new set V-S representing LSFT. The addition of stylolite roughness inversion not only allows refining the deformation history but also provides a rare high-resolution insight into the evolution of both tectonic stress and burial depth in a constrainable chronological frame.

An estimate of the rate of erosion at the fold hinge during hinge amplification and related erosion can help test if the hypothesis of 900 to 1600 m of sediment deposition from the hinge is reasonable. The reconstruction of syntectonic sediment deposition in the MNA suggests that folding in the western UMAR occurred during the Tortonian [Barchi *et al.*, 2012]. In the absence of more accurate estimates, one can consider that hinge amplification occurred roughly over 2 Ma, which is the duration of the Tortonian stage. In this case, considering that most of the eroded sediments were deposited in the backlimb of the fold (hence assuming that few eroded material was carried away along fold-strike) and that the erosion rate is analogous to the exhumation rate, this rate is in the order of 0.9 km/Ma. Apatite fission track (FT) analysis of the UMAR show a rapid cooling (25°C/Ma), suggesting an exhumation rate of about 0.9 km/Ma in the eastern Altotiberina extensional fault system [Caricchi *et al.*, 2015a] to 1 km/Ma in the eastern Romagna-Umbria during the Messinian time [Zattin, 1999]. In the northern Apennines, where the Ligurian nappes have overthrust the competent core, a combination of vitrinite reflectance analysis and zircon and apatite FT analysis predicts an exhumation rate of about 0.5 km/Ma [Ventura *et al.*, 2001]. More recent AFT studies reconstructed a Miocene exhumation rate of 0.9–1 km/Ma in the northern Apennines [Thomson *et al.*, 2010]. Both values are similar to our estimates to a first order. That tends to support our interpretation of a local overburden in the backlimb due to the deposition of the material eroded from the hinge (Figure 9). The existence of large burial depths suggests that dissolution has been active still after folding on some of the BPS planes, implying a permutation of the maximum principal stress from a horizontal  $\sigma_1$  to a vertical  $\sigma_1$ .

## 5.2. Sequence of Deformation in the MNA

Fracture and stylolite populations at the fold scale show four joint/vein and three tectonic stylolite sets. Calcite twin inversion results show six successive stress tensors. Joint/vein sets distribution is not related to the stratigraphic column, and each is observed in every sedimentary group considered, which supports our conclusion that they developed after the compaction of the whole competent core and consequently do not reflect events predating Miocene times as some normal faults may do [Marchegiani *et al.*, 1999]. Based on the chronological relationships observed in the field and inferred from calcite twinning analysis, we propose a deformation sequence that illustrates the polyphase tectonic history spanning from fold-unrelated events predating fold growth to the fold-unrelated events postdating fold growth. This classification refines the successive steps proposed by Beaudoin *et al.* [2012] and is as follows: the prefolding events refer to all events predating folding related to a stress field that is not responsible for fold development. These events potentially include (1) any development of compressional/extensional structures related to deformation phases older than the Apenninic compression and (2) prefolding Layer-Parallel Shortening (LPS) under a stress field not consistent with folding but related to regional Apenninic compression. The next events reflect folding-related deformation steps, as described in more detail in Tavani *et al.* [2015]: (3) early-folding LPS which is a LPS deformation phase under a stress field compatible with strata tilting due to folding, (4) the synfolding parallel and transvers stretching with strata bending at the hinge, and (5) the late-stage fold tightening (LSFT) when the fold limbs are locked and shortening is still consistent with the folding. Folding is followed by postfolding events: (6) other postfolding deformation triggered by a stress field not consistent with the one under which folding occurred, referred to as postfolding events, and sometimes (7) gravity-driven extension. In our case the term “postfolding event” refers to step 7. The tectonic history of the MNA as we interpret it is illustrated in Figure 10, with stages named with respect to this classification.

Joint-vein sets I and II striking N020 to N050 and related stylolite set II-S affect the whole structure and all formations and are related to strike-slip and subsequent compressional N045  $\sigma_1$ -trending stress tensors as revealed by calcite twin inversion. These microstructures can be related to the regional Apenninic compression associated with  $\sigma_1$  trending NE-SW that formed the UMAR [Marshak *et al.*, 1982; Storti and Salvini, 2001; Billi *et al.*, 2007; Tavani *et al.*, 2008; Barchi *et al.*, 2012]. The 20/30° variation in compression direction between sets I and II may be related to a counterclockwise regional- or fold-scale strata rotation around a vertical axis. Such a regional rotation has not been proposed in the innermost part of the UMAR, mainly because of the structural complexity of the area [Lowrie and Hirt, 1988; Channell, 1992; Tavani and Cifelli, 2010]. Several studies illustrate a 15° to 20° counterclockwise rotation around a vertical axis in the pre-UMAR (east of UMAR [Channell, 1992]) and south of the UMAR (Sabina Latium-Abruzzi anticline, [Mattei *et al.*, 1995; Tavani and Cifelli, 2010]), which fits with our interpretation supported by other examples where the strata rotation in map view is recorded by the fracture network distribution [e.g., Beaudoin *et al.*, 2015]. Such a stress

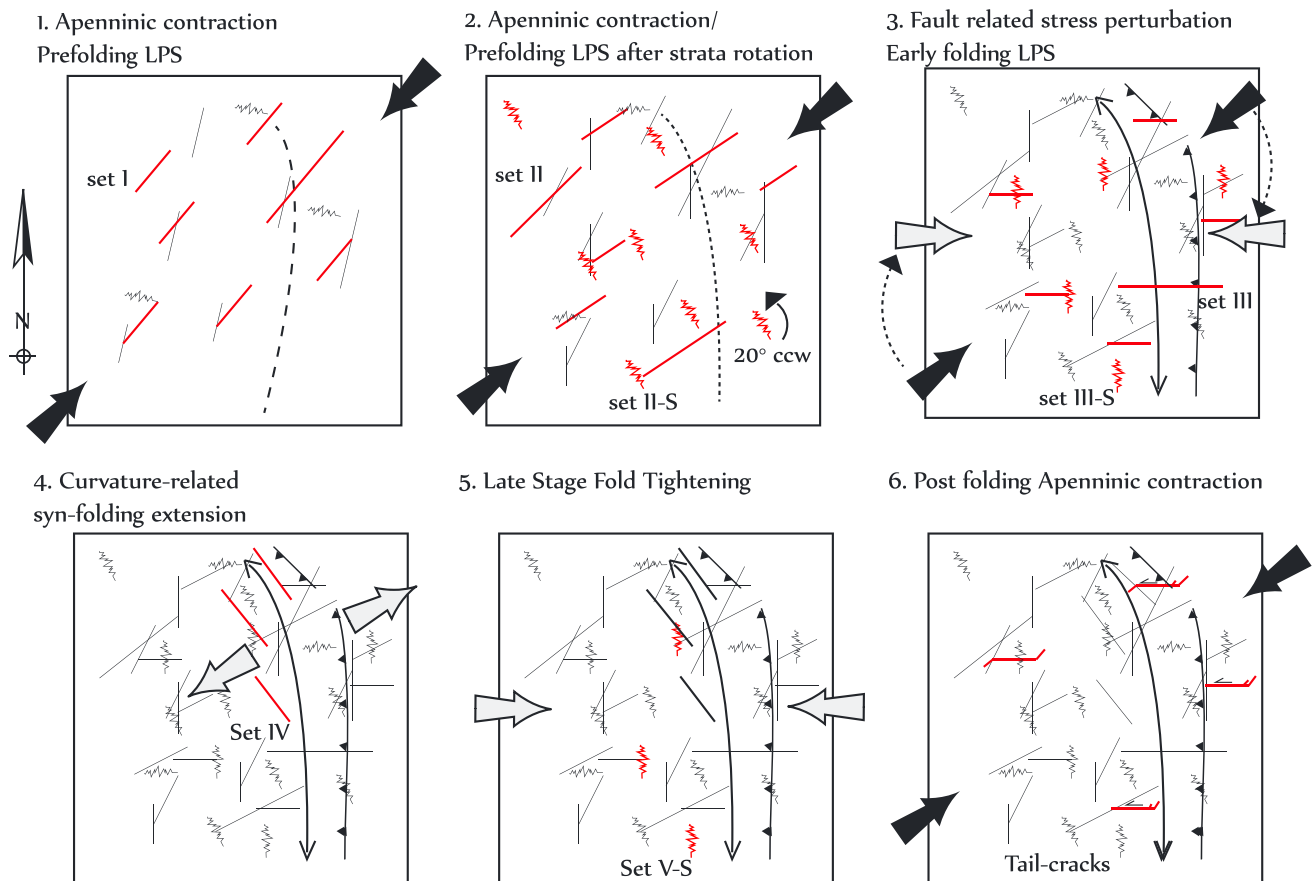


**Figure 10.** Map-view sketches of the main horizontal stress direction and mesostructure development at the scale of the MNA. Seven stages are reported to include all the reconstructed tectonic events. The black arrows show the regional direction of the stress, while the grey arrows indicate the local stress directions. Developing mesostructures during each stage are highlighted in red. Reported names for steps refer to the description of section 5.1. in the text. Abundance or relative length is not represented in this figure.

rotation in map view can also be related to a large-scale geodynamic evolution that led to the arcuate-shape of the UMAR [Calamita and Deiana, 1988]. The development of vein/joint set II and III is interpreted as the prefolding LPS substage as the fold axis is curved in map view and trends closer to N180. The N040 trend of the compressional stress is not perpendicular to the axis of the fold and is believed to reflect regional-scale stress and is consequently not compatible with the folding, which occurred under a N090 compressional trend (Figure 10, stages 1–2).

The next event is associated with E-W (080–110) striking joint/vein set III, ~E-W  $\sigma_1$ -trending compressional and strike-slip compatible stress tensors and ~E-W trending tectonic stylolite teeth of set III-S. We interpret this to represent early-folding with a ~E-W compression that developed due to a perturbation of the regional Apenninic compression caused by the reactivation of the N180 striking fault that controls the structure of the MNA (Figure 10, stage 3). This fault is likely an inherited fault that developed during Jurassic rifting. Reactivated inherited faults at depth can induce stress perturbations in the overlying strata as soon as they accommodate deformation [e.g., Bellahsen et al., 2006b; Amrouch et al., 2011]. Such a fold-scale perturbation of the regional stress direction induced by an oblique inherited structure has been illustrated in other folds [Varga, 1993; Homberg et al., 1997]. Sets III and III-S teeth are roughly perpendicular to the axis of the fold and may then be related to the LPS early-folding substage, broadly described in several fold-thrust belts [Evans and Dunne, 1991; Rocher et al., 2000; Bellahsen et al., 2006a; Lacombe et al., 2006; Quintà and Tavani, 2012; Weil and Yonkee, 2012; Chu et al., 2013; Tavani et al., 2015].

N135 striking joint/vein set IV is compatible with an extensional stress tensor with a horizontal  $\sigma_3$  trending NE-SW as reconstructed from calcite twin analysis with horizontal  $\sigma_3$  striking from NE-SW to E-W. Because



of (1) the lack of associated consistent contractional features (stylolites), (2) the absence of consistent compressional or strike-slip compatible stress tensors recorded by calcite twinning, and (3) the location of this stress mainly at the hinge of the fold (Figure 5) and (4) the arcuate shape of the fold, one can consider that this joint/vein set is associated with synfolding extension related to strata bending and tilting/curvature in the backlimb. This falls in the so-called synfolding strata bending deformation stage (Figure 10, stage 4), and thus, those features can be considered to develop after the LPS stage, and after both prefolding and early folding stages.

The subsequent event is given by calcite twin analysis and by tectonic stylolite developing in the forelimb at an anomalous depth, related to the overturning of the strata. That set V-S develops under an E-W striking  $\sigma_1$ , still consistent with the stress field under which the MNA developed. These microstructures then fall in the LSFT (Figure 10, stage 5) and cannot be unambiguously recognized from fracture network observation only, because bed-perpendicular fractures that are oriented perpendicular to the bedding's strike remain vertical irrespective of strata-tilting. This set V-S is characterized by both compressional and strike-slip stress regimes, given from calcite twins and stylolite roughness, respectively.

A second posttilting event recorded in the data set is related to the occurrence of tail-cracks on the N090 striking fracture set III indicating a NE-SW contraction, supported by calcite twins inversion of sites 118 (T2) and 161 (T1) that shows a post folding NE-SW striking  $\sigma_1$  (Figure 7 and Table 1). This event is not anymore compatible with the E-W stress field that developed the fold and falls in the postfolding stage of deformation (Figure 10, stage 6). This event indicates that the regional Apenninic stress that was prevailing during the pre-folding stage is seen postfolding and the stress is no longer perturbed by the N180 fault. This interpretation is consistent with the development of a north-eastward directed piggyback sequence of the UMAR belt [Bally *et al.*, 1986; Calamita and Deiana, 1988], and suggests that the MNA ceased to be active while the outermost folds of the UMAR developed in the east [Barchi *et al.*, 2012].

### 5.3. Stress History During the Growth of the MNA

Differential stress magnitudes derived from stylolite roughness inversion (Table 3) can be compared to the maximum differential stresses reconstructed from calcite twin inversion (Table 1). The comparison highlights that differential stress magnitudes given by both methods are remarkably close (Figure 9), from 30 to 106 MPa for calcite and from 33 to 97 MPa for stylolite. This stands for all stylolites but for the four tectonic stylolites that give back a minimum crossover length that is lower than  $10^{-2}$  mm. In that case, the reconstructed differential stress values seem unreasonable, with a  $\sigma_{dmax}$  reaching up to 500 MPa. The extreme values suggest that a stylolite with a value of  $L_c$  that is smaller than  $10^{-2}$  mm may not be used as a paleopiezometer. This limitation may be related to the limited resolution during data acquisition and image treatment or to a complex interaction between pinning particles and surface energy at this scale, which may lead to a breakdown of the growth equation proposed by Schmittbuhl *et al.* [2004]. We then discarded these data as they are more likely to reflect an artefact of the method rather than actual paleostress magnitudes.

If we discard these four stylolites, the consistency between maximum differential stresses reconstructed independently from both methods suggests that tectonic stylolites can be used as reliable paleopiezometers [Ebner *et al.*, 2010b] to reconstruct stress magnitudes, even at great depth and in complex tectonic settings. Results show that tectonic stylolites can form in horizontal strata (as LPS-related stylolites for instance) under both strike-slip compatible and compressional stress regimes and that even if they are spatially associated with bed-perpendicular joint/vein sets normal to considered stylolites, they cannot be systematically considered as representative of a bed perpendicular  $\sigma_2$ , as it is classically done in structural geology. Our results unambiguously show that without carrying out roughness inversion the only indication tectonic stylolite can give is strictly the orientation of  $\sigma_1$ .

If we look at a stage-by-stage comparison between calcite twins and stylolite roughness paleopiezometers (Figure 9), results for values of  $\sigma_{dmax}$  are close. For the prefolding LPS (sets I/II/II-S),  $\sigma_{dmax}$  values reconstructed from stylolites range from 33 to 77 MPa and from 26 to 106 MPa from calcite twinning inversion. For the early-folding LPS (set III/III-S),  $\sigma_{dmax}$  values range from 33 to 46 MPa from stylolites, while calcite twins give values from 33 to 56 MPa. Finally, the LSFT (set V-S) is characterized by a  $\sigma_{dmax}$  value range of 70 to 97 MPa from stylolites and 40 to 64 MPa from calcite twins. These comparable values support that tectonic stylolite

roughness inversion is an efficient and meaningful paleopiezometer. However, the combination of both techniques shows that the stress regimes are not the same during the same tectonic stage. Because stylolites and veins show complex chronological relationships, we think that stylolites and veins can develop in alternation or under the same regime. This implies that during the same tectonic stage (for instance early folding LPS), the stress regime is likely to switch more than once from compressional to strike-slip compatible, leading to a phenomenon that we can call stress regime oscillation. It is striking to notice that these regime changes occur with very few changes of the  $\sigma_{dmax}$ , suggesting the oscillation is not directly related to stress build-up but rather to an anisotropic evolution of horizontal principal stresses, as shown by the reconstruction of the absolute magnitude of  $\sigma_H$ ,  $\sigma_{hr}$ , and  $\sigma_v$ , i.e., the maximum horizontal stress, minimum horizontal stress, and vertical stress, respectively (Table 3). Such a stress evolution during thrusting and folding challenges the commonly reported model of stress build-up during LPS with stress permutations from strike-slip to compressional possibly related to the compressional reactivation of an inherited fault [e.g., *Amrouch et al.*, 2010; *Beaudoin et al.*, 2012; *Tavani et al.*, 2015]. This finding rather supports models that predict complex stress regime evolution during deformation, related to anisotropy in the upper crust, or due to fluid overpressure [Cosgrove, 1997; Hu and Angelier, 2004; Mourgues and Cobbold, 2003, 2006; Tavani et al., 2015].

## 6. Conclusion

In this work we show how bed-parallel and tectonic stylolites, veins/fractures, and calcite twins can be used in a combined approach to reconstruct a detailed paleostress history enabling fingerprinting of stress orientations, stress permutations, and stress magnitudes. To do so, we report a new and easy-to-use method to perform tectonic stylolite roughness inversion that does not require an access to an open stylolite surface. We use the Monte Nero Anticline in the Umbria Marches Arcuate Ridge of the northern Apennines as case study.

The polyphase tectonic history reconstructed from mesostructure and microstructure in the MNA consists of (1) a prefolding LPS under a stress direction N045 showing a possible local rotation of strata in a map view counterclockwise sense, (2) an early-folding LPS where stress direction is locally perturbed toward a N090 trend by the compressional reactivation of a N180 striking inherited normal fault beneath the fold as a high-angle thrust, (3) curvature-related extension, (4) LSFT, and (5) postfolding deformation under a compressive stress direction of N045.

The reconstruction of the depth of formation of the sedimentary stylolites along with mathematical constraints given by the roughness inversion of some tectonic stylolites allows the reconstruction of the burial history of strata during folding with a high resolution: a local synfolding burial of both limbs of the fold is deduced from burial history, with burial increasing from 2700 m to 4300 m during folding. This effect is interpreted as resulting from (1) deposition of the material eroded from the developing hinge on the backlimb and (2) the overturning of strata in the forelimb. Our results highlight that stylolite 3-D roughness inversion is an adapted technique even for stylolites that are active up to 4300 m depth, which is shown here for the first time. Getting such a high-resolution stress history from the fracture-stylolite network itself is a major addition to fold-fracture studies that cannot properly estimate burial evolution during folding without using a separate paleobarometer (like oil-bearing fluid inclusions [e.g., *Roure et al.*, 2010]).

The similarity of the order of magnitude of the reconstructed differential stress values from calcite twin and stylolite stress inversion underpins that the inversion of tectonic stylolite roughness is a robust paleopiezometer. Our study also illustrates limits of the inversion method: if one of the reconstructed values of the crossover length is smaller than  $10^{-2}$  mm, then the stylolite cannot be considered as a reliable paleopiezometer, at least with the resolution that we used for the method.

Because the method allows calculations of stress regimes and of stress magnitudes for several deformation steps, the combination of stylolite 3-D roughness and calcite twinning paleopiezometry sheds light on a number of mechanisms involved in fold-stress models:

1. Even when they are temporally associated with a vein/joint set, stylolite teeth alone cannot be used as indicators for a strike-slip versus compression compatible stress regimes, since stylolites with the same orientation could have developed under both regimes. Only a 3-D roughness inversion reveals the full stress regime under which a stylolite developed.

2. Stress regimes may oscillate between compressional and strike-slip during each stage of fold development, so that stress magnitude evolution appears likely to be nonlinear showing anisotropic evolution in the horizontal plane. This behavior has never been assessed at this scale before and shows that stress history reconstruction must be done at the highest resolution possible to reveal its complexity and better understand its evolution.

Beyond regional implications, this work highlights that the analysis of sedimentary and tectonic stylolites in combination with an analysis of fracture/vein sets and calcite twins provides a new powerful toolbox to accurately unravel paleostress fingerprinting in basins and orogens. The outcome of this study opens ways to a rethinking of the stress evolution during long-lasting deformation.

## Appendix A

This part presents the derivation that leads from equation (4) to equations (5.1)–(5.3) that are used to reconstruct the evolution of the crossover length  $L_c$  regarding the angle  $\theta$  in a case of a stress anisotropy on the stylolite plane (see section 3.3.2 of the main text).

Considering the equation of a periodic function of period  $\pi$  (all angles must be express in radians for the calculations):

$$Lc(\theta) = a + b\sin(2\theta + c), \quad (A1)$$

Considering three couples  $[\theta, L_c]_{1,2,3}$  reconstructed along three cuts on the tectonic stylolite (Figure 6b), we have the following system of equations:

$$Lc_{(\theta_{1,2,3})} = a + b\sin(2\theta_{1,2,3} + c), \quad (A2)$$

Parameter  $a$  expresses as follow from equation (A1):

$$a = Lc_1 - b\sin(2\theta_1 + c), \quad (A3a)$$

Replacing  $a$  in the equation (A2) by its expression (A3a):

$$\begin{aligned} Lc_2 &= Lc_1 - b\sin(2\theta_1 + c) + b\sin(2\theta_2 + c), \\ \leftrightarrow b &= \frac{(Lc_2 - Lc_1)}{\sin(2\theta_2 + c) - \sin(2\theta_1 + c)}, \end{aligned} \quad (A3b)$$

Replacing  $a$  in the equation (A2) by its expression (A3a):

$$\begin{aligned} Lc_3 &= Lc_1 - b\sin(2\theta_1 + c) + b\sin(2\theta_3 + c), \\ \leftrightarrow \frac{Lc_3 - Lc_1}{b} &= -\sin(2\theta_1 + c) + \sin(2\theta_3 + c) \end{aligned}$$

Then replacing  $b$  by its expression (A3b):

$$\leftrightarrow \frac{Lc_2 - Lc_1}{Lc_3 - Lc_1} = \frac{(\sin(2\theta_2 + c) - \sin(2\theta_1 + c))}{\sin(2\theta_3 + c - \sin(2\theta_1 + c))}$$

If  $\frac{Lc_2 - Lc_1}{Lc_3 - Lc_1} = \Delta L$ ,

$$\begin{aligned} \leftrightarrow \Delta L \cos c (\sin 2\theta_3 - \sin 2\theta_1) + \Delta L \operatorname{sinc}(\cos 2\theta_3 - \cos 2\theta_1) \\ = \cos c (\sin 2\theta_2 - \sin 2\theta_1) + \sin c (\cos 2\theta_2 - \cos 2\theta_1) \\ \leftrightarrow 0 &= \cos c (\Delta L (\sin 2\theta_3 - \sin 2\theta_1) - (\sin 2\theta_2 - \sin 2\theta_1)) \\ &\quad + \sin c (\Delta L (\cos 2\theta_3 - \cos 2\theta_1) - (\cos 2\theta_2 - \cos 2\theta_1)) \\ \leftrightarrow \frac{\sin c}{\cos c} &= -\frac{\Delta L (\sin 2\theta_3 - \sin 2\theta_1) - (\sin 2\theta_2 - \sin 2\theta_1)}{\Delta L (\cos 2\theta_3 - \cos 2\theta_1) - (\cos 2\theta_2 - \cos 2\theta_1)} \end{aligned}$$

That leads to equation (5.3)

$$c = \tan^{-1} \left( -\frac{\Delta L (\sin 2\theta_3 - \sin 2\theta_1) - (\sin 2\theta_2 - \sin 2\theta_1)}{\Delta L (\cos 2\theta_3 - \cos 2\theta_1) - (\cos 2\theta_2 - \cos 2\theta_1)} \right)$$

## Acknowledgments

Authors wish to thank R. Toussaint for stimulating discussions and M. Fondriest and S. Siman Tov for their help on the field. We thank S. Tavani, an anonymous reviewer, and the Associate Editor P. Vannuchi for their comments that greatly improved the quality of the manuscript. This work has received funding from the European Union's Seventh Framework Programme for research, technological development, and demonstration under grant agreement 316889. All data used in this paper are available upon demand to the main author (Nicolas.beaudoin@glasgow.ac.uk).

## References

- Ahmadhadi, F., O. Lacombe, and J.-M. Daniel (2007), Early reactivation of basement faults in Central Zagros (SW Iran): Evidence from pre-folding fracture populations in Asmari formation and Lower Tertiary Paleogeography, in *Thrust Belt and Foreland Basins*, pp. 205–228, Springer, Berlin.
- Ahmadhadi, F., J.-M. Daniel, M. Azzizadeh, and O. Lacombe (2008), Evidence for pre-folding vein development in the Oligo-Miocene Asmari formation in the Central Zagros fold belt, Iran, *Tectonics*, *27*, TC1016, doi:10.1029/2006TC001978.
- Alvarez, W., T. Engelder, and W. Lowrie (1976), Formation of spaced cleavage and folds in brittle limestone by dissolution, *Geology*, *4*, 698–701, doi:10.1130/0091-7613(1976)4<698:FOSCAF>2.0.CO;2.
- Alvarez, W., T. Engelder, and P. A. Geiser (1978), Classification of solution cleavage in pelagic limestones, *Geology*, *6*(5), 263–266, doi:10.1130/0091-7613(1978)6<263.
- Amrouch, K., O. Lacombe, N. Bellahsen, J.-M. Daniel, and J.-P. Callot (2010), Stress and strain patterns, kinematics and deformation mechanisms in a basement-cored anticline: Sheep Mountain Anticline, Wyoming, *Tectonics*, *29*, TC1005, doi:10.1029/2009TC002525.
- Amrouch, K., N. Beaudoin, O. Lacombe, N. Bellahsen, and J.-M. Daniel (2011), Paleostress magnitudes in folded sedimentary rocks, *Geophys. Res. Lett.*, *38*, L17301, doi:10.1029/2011GL048649.
- Anderson, E. M. (1951), *The Dynamic of Faulting*, Oliver & Boyd, Edinburgh, U. K.
- André, A.-S., J. Sausse, and M. Lespinasse (2001), New approach for the quantification of paleostress magnitudes: Application to the Soultz vein system (Rhine graben, France), *Tectonophysics*, *336*(1–4), 215–231, doi:10.1016/S0040-1951(01)00103-2.
- Angelier, J. (1989), From orientation to magnitudes in paleostress determinations using fault slip data, *J. Struct. Geol.*, *11*(1–2), 37–50, doi:10.1016/0191-8141(89)90034-5.
- Arthaud, F., and M. Mattauer (1969), Exemples de stylolites d'origine tectonique dans le Languedoc, leur relation avec la tectonique cassante, *Bull. Soc. Geol. Fr.*, *11*, 738–744.
- Asaro, R., and W. Tiller (1972), Interface morphology development during stress corrosion cracking: Part 1, Via surface diffusion, *Metall. Trans.*, *3*, 1789–1796.
- Bally, A. W., L. Burbi, C. Cooper, and R. Ghelardoni (1986), Balanced sections and seismic reflection profiles across the Central Apennines, *Mem. Soc. Geol. Ital.*, *35*, 257–310.
- Barchi, M. R., W. Alvarez, and D. H. Shimabukuro (2012), The Umbria-Marche Apennines as a double orogen: Observations and hypotheses, *Ital. J. Geosci.*, *131*(2), 258–271, doi:10.3301/IJG.2012.17.
- Beaudoin, N., R. Leprêtre, N. Bellahsen, O. Lacombe, K. Amrouch, J. P. Callot, L. Emmanuel, and J. M. Daniel (2012), Structural and microstructural evolution of the Rattlesnake Mountain Anticline (Wyoming, USA): New insights into the Sevier and Laramide orogenic stress build-up in the Bighorn Basin, *Tectonophysics*, *576–577*, 20–45, doi:10.1016/j.tecto.2012.03.036.
- Beaudoin, N., D. Huyghe, N. Bellahsen, O. Lacombe, L. Emmanuel, F. Mouthereau, and L. Ouahnon (2015), Fluid systems and fracture development during syn-depositional fold growth: An example from the Pico del Aguila anticline, Sierras Exteriores, southern Pyrenees, Spain, *J. Struct. Geol.*, *70*(C), 23–38, doi:10.1016/j.jsg.2014.11.003.
- Bellahsen, N., P. E. Fiore, and D. D. Pollard (2006a), From spatial variation of fracture patterns to fold kinematics: A geomechanical approach, *Geophys. Res. Lett.*, *33*, L02301, doi:10.1029/2005GL024189.
- Bellahsen, N., P. Fiore, and D. D. Pollard (2006b), The role of fractures in the structural interpretation of Sheep Mountain Anticline, Wyoming, *J. Struct. Geol.*, *28*(5), 850–867, doi:10.1016/j.jsg.2006.01.013.
- Bergbauer, S., and D. D. Pollard (2004), A new conceptual fold-fracture model including pre-folding joints, based on the Emigrant Gap anticline, Wyoming, *GSA Bull.*, *116*(3/4), 294–307.
- Billi, A., et al. (2006), First results from the CROP-11 deep seismic profile, central Apennines, Italy: Evidence of mid-crustal folding, *J. Geol. Soc.*, *163*(4), 583–586, doi:10.1144/0016-764920-002.
- Billi, A., A. Valle, M. Brilli, C. Faccenna, and R. Funicello (2007), Fracture-controlled fluid circulation and dissolutional weathering in sinkhole-prone carbonate rocks from central Italy, *J. Struct. Geol.*, *29*(3), 385–395, doi:10.1016/j.jsg.2006.09.008.
- Bons, P., M. Elburg, and E. Gomez-Rivas (2012), A review of the formation of tectonic veins and their microstructures, *J. Struct. Geol.*, *43*, 33–62, doi:10.1016/j.jsg.2012.07.005.
- Calamita, F., and G. Deiana (1988), The arcuate shape of the Umbria-Marche-Sabina Apennines (central Italy), *Tectonophysics*, *146*(1–4), 139–147, doi:10.1016/0040-1951(88)90087-X.
- Caricchi, C., L. Aldega, and S. Corrado (2015a), Reconstruction of maximum burial along the Northern Apennines thrust wedge (Italy) by indicators of thermal exposure and modeling, *Geol. Soc. Am. Bull.*, *127*, 428–442, doi:10.1130/B30947.1.
- Caricchi, C., L. Aldega, M. R. Barchi, S. Corrado, D. Grigo, F. Mirabella, and M. Zattin (2015b), Exhumation patterns along shallow low-angle normal faults: An example from the Alotiberina active fault system (Northern Apennines, Italy), *Terra Nova*, *27*(4), 312–321, doi:10.1111/ter.12163.
- Carminati, E., M. Lustrino, M. Cuffaro, and C. Doglioni (2010), Tectonics, magmatism and geodynamics of Italy: What we know and what we imagine, *J. Virtual Explor.*, *36*, 9, doi:10.3809/jvirtex.2009.00226.
- Casini, G., et al. (2011), Sub-seismic fractures in foreland fold and thrust belts: Insight from the Lurestan Province, Zagros Mountains, Iran, *Pet. Geosci.*, *17*, 263–282, doi:10.1144/1354-079310-043.
- Channell, J. (1992), Paleomagnetic data from Umbria (Italy): Implications for the rotation of Adria and Mesozoic apparent polar wander paths, *Tectonophysics*, *216*, 365–378.
- Chu, H.-T., J.-C. Lee, F. Bergerat, J.-C. Hu, S.-H. Liang, C.-Y. Lu, and T.-Q. Lee (2013), Fracture patterns and their relations to mountain building in a fold-thrust belt: A case study in NW Taiwan, *Bull. Soc. Geol. Fr.*, *184*(4–5), 485–500, doi:10.2113/gssgfbull.184.4-5.485.
- Clark, S. P. J. (1966), *Handbook of Physical Constants*, Geol. Soc. of New York, New York.
- Cooke, M. (1997), Fracture localization along faults with spatially varying friction, *J. Geophys. Res.*, *102*, 22,425–22,434, doi:10.1029/97JB01829.
- Cooper, S. P., L. B. Goodwin, and J. C. Lorenz (2006), Fracture and fault patterns associated with basement-cored anticlines: The example of Teapot Dome, Wyoming, *AAPG Bull.*, *90*, 1903–1920.
- Cosgrove, J. W. (1997), The influence of mechanical anisotropy on the behaviour of the lower crust, *Tectonophysics*, *280*(1–2), 1–14, doi:10.1016/S0040-1951(97)00145-5.
- Deiana, G., G. Cello, M. Chiochini, S. Galdenzi, S. Mazzoli, E. Pltostoli, M. Potetti, A. Romano, E. Turco, and M. Principi (2002), Tectonic evolution of the external zones of the Umbria-Marche Apennines in the Monte San Vicino-Cingoli area, *Boll. Soc. Geol. Ital.*, *1*, 229–238.
- Ebner, M. (2009), The development of stylolites, from small-scale heterogeneities to multi-scale roughness, 125 pp., Mainz Univ.
- Ebner, M., D. Koehn, R. Toussaint, F. Renard, and J. Schmittbuhl (2009), Stress sensitivity of stylolite morphology, *Earth Planet. Sci. Lett.*, *277*(3–4), 394–398, doi:10.1016/j.epsl.2008.11.001.
- Ebner, M., S. Piazzolo, F. Renard, and D. Koehn (2010a), Stylolite interfaces and surrounding matrix material: Nature and role of heterogeneities in roughness and microstructural development, *J. Struct. Geol.*, *32*(8), 1070–1084, doi:10.1016/j.jsg.2010.06.014.



- Ebner, M., R. Toussaint, J. Schmittbuhl, D. Koehn, and P. Bons (2010b), Anisotropic scaling of tectonic stylolites: A fossilized signature of the stress field?, *J. Geophys. Res.*, *115*, B06403, doi:10.1029/2009JB006649.
- Elter, P., G. Giglia, M. Tongiorgi, and L. Trevisan (1975), Tensional and compressional areas in the recent (Tortonian to present) evolution of the Northern Apennines, *Boll. Geofis. Teor. Appl.*, *42*, 3–18.
- Engelder, T. (1987), Joints and some fractures in rocks, in *Fracture Mechanics of Rocks*, edited by B. Atkinson, pp. 27–69, Academic Press, London.
- Engelder, T., P. A. Geiser, and W. Alvarez (1981), Role of pressure solution and dissolution in geology, *Geology*, *9*(1), 44–45, doi:10.1130/0091-7613(1981)9<44:ropsad>2.0.co;2.
- Etchecopar, A. (1984), Etude des états de contraintes en tectonique cassante et simulation de déformations plastiques, 270 pp., Univ. of Montpellier.
- Evans, M. A., and W. M. Dunne (1991), Strain factorization and partitioning in the North Mountain thrust sheet, central Appalachians, U.S.A., *J. Struct. Geol.*, *13*, 21–35.
- Faulkner, D. R., C. A. L. Jackson, R. J. Lunn, R. W. Schlische, Z. K. Shipton, C. A. J. Wibberley, and M. O. Withjack (2010), A review of recent developments concerning the structure, mechanics and fluid flow properties of fault zones, *J. Struct. Geol.*, *32*(11), 1557–1575, doi:10.1016/j.jsg.2010.06.009.
- Ferrill, D. A., A. P. Morris, M. A. Evans, M. Burkhard, R. H. Groshong, and C. M. Onasch (2004), Calcite twin morphology: A low-temperature deformation geothermometer, *J. Struct. Geol.*, *26*(8), 1521–1529, doi:10.1016/j.jsg.2003.11.028.
- Fischer, M., N. Woodward, and M. Mitchell (1992), The kinematics of break-thrust folds, *J. Struct. Geol.*, *14*(4), 451–460, doi:10.1016/0191-8141(92)90105-6.
- Gratier, J. P., and R. Guiguet Irigm (1986), Experimental pressure solution-deposition on quartz grains: The crucial effect of the nature of the fluid, *J. Struct. Geol.*, *8*(8), 845–856, doi:10.1016/0191-8141(86)90030-1.
- Gratier, J.-P., P. Favreau, and F. Renard (2003), Modeling fluid transfer along California faults when integrating pressure solution crack sealing and compaction processes, *J. Geophys. Res.*, *108*(B2), 2104, doi:10.1029/2001JB000380.
- Gratier, J. P., L. Muquet, R. Hassani, and F. Renard (2005), Experimental microstylolites in quartz and modeled application to natural stylolitic structures, *J. Struct. Geol.*, *27*(1), 89–100, doi:10.1016/j.jsg.2004.05.007.
- Heap, M. J., P. Baud, T. Reuschle, and P. G. Meredith (2014), Stylolites in limestones: Barriers to fluid flow?, *Geology*, *42*(1), 51–54, doi:10.1130/G34900.1.
- Heidbach, O., K. Fuchs, B. Muller, F. Wenzel, J. Reinecker, M. Tingay, and B. Sperner (2007), The world stress map.
- Homberg, C., J. C. Hu, J. Angelier, F. Bergerat, and O. Lacombe (1997), Characterization of stress perturbations near major fault zones: Insights from 2-D distinct-element numerical modelling and field studies (Jura mountains), *J. Struct. Geol.*, *19*(5), 703–718, doi:10.1016/S0191-8141(96)00104-6.
- Hu, J.-C., and J. Angelier (2004), Stress permutations: Three-dimensional distinct element analysis accounts for a common phenomenon in brittle tectonics, *J. Geophys. Res.*, *109*, B09403, doi:10.1029/2003JB002616.
- Jacobacci, A. (1979), Carte Geologica d'Italia, foglio 301: Servizio Geologico d'Italia, 1:25.000.
- Jamison, W. R., and J. H. Spang (1976), Use of calcite twin lamellae to infer differential stress, *GSA Bull.*, *87*, 868–872.
- Koehn, D., F. Renard, R. Toussaint, and C. Passchier (2007), Growth of stylolite teeth patterns depending on normal stress and finite compaction, *Earth Planet. Sci. Lett.*, *257*(3–4), 582–595, doi:10.1016/j.epsl.2007.03.015.
- Koehn, D., M. Ebner, F. Renard, R. Toussaint, and W. Passchier (2012), Modelling of stylolite geometries and stress scaling, *Earth Planet. Sci. Lett.*, *341*, 104–113, doi:10.1016/j.epsl.2012.04.046.
- Kohlstedt, D. L., and M. S. Weathers (1980), Deformation-induced microstructures, paleopiezometers, and differential stresses in deeply eroded fault zones, *J. Geophys. Res.*, *85*, 6269–6285, doi:10.1029/JB085iB11p06269.
- Lacombe, O. (2001), Paleostress magnitudes associated with development of mountain belts: Insights from tectonic analyses of calcite twins in the Taiwan Foothills, *Tectonics*, *20*, 834–849, doi:10.1029/2001TC900019.
- Lacombe, O. (2007), Comparison of paleostress magnitudes from calcite twins with contemporary stress magnitudes and frictional sliding criteria in the continental crust: Mechanical implications, *J. Struct. Geol.*, *29*, 86–99, doi:10.1016/j.jsg.2006.08.009.
- Lacombe, O. (2010), Calcite twins, a tool for tectonic studies in thrust belts and stable orogenic forelands, *Oil Gas Sci. Technol.*, *65*(6), 809–838.
- Lacombe, O., and P. Laurent (1992), Determination of principal stress magnitudes using calcite twins and rock mechanics data, *Tectonophysics*, *202*, 83–93.
- Lacombe, O., J. Angelier, P. Laurent, F. Bergerat, and C. Tournier (1990), Joint analyses of calcite twins and fault slips as a key for deciphering polyphase tectonics: Burgundy as a case study, *Tectonophysics*, *182*, 279–300.
- Lacombe, O., J. Angelier, M. Rocher, J. Bergues, H.-T. Chu, B. Deffontaines, and J.-C. Hu (1996), Stress patterns associated with folding at the front of a collision belt: Example from the Pliocene reef limestones of Yutengping (Taiwan), *Bull. Soc. Géol. Fr.*, *167*(3), 361–374.
- Lacombe, O., F. Mouthereau, S. Kargar, and B. Meyer (2006), Late Cenozoic and modern stress fields in the western Fars (Iran): Implications for the tectonic and kinematic evolution of Central Zagros, *Tectonics*, *25*, TC1003, doi:10.1029/2005TC001831.
- Lacombe, O., K. Amrouch, F. Mouthereau, and L. Dissez (2007), Calcite twinning constraints on late Neogene stress patterns and deformation mechanisms in the active Zagros collision belt, *Geology*, *35*(3), 263–266.
- Lacombe, O., N. Bellahsen, and F. Mouthereau (2011), Fracture patterns in the Zagros simply folded belt (Fars): New constraints on early collisional tectonic history and role of basement faults, *Geol. Mag.*, *148*(5–6), 940–963, doi:10.1017/S001675681100029X.
- Laubach, S. E. (1988), Subsurface fractures and their relationship to stress history in East Texas basin sandstone, *Tectonophysics*, *156*(1–2), 37–49.
- Laubach, S. E. (1989), Paleostress directions from the preferred orientation of closed microfractures (fluid-inclusion planes) in sandstone, East Texas basin, U.S.A., *J. Struct. Geol.*, *11*(5), 603–611.
- Laubach, S. E., J. E. Olson, and J. F. W. Gale (2004), Are open fractures necessarily aligned with maximum horizontal stress?, *Earth Planet. Sci. Lett.*, *222*(1), 191–195.
- Laurent, P., H. Kern, and O. Lacombe (2000), Determination of deviatoric stress tensors based on inversion of calcite twin data from experimentally deformed monophase samples. II: Uniaxial and triaxial stress experiments, *Tectonophysics*, *327*, 131–148.
- Lavecchia, G., G. Minelli, and G. Piali (1988), The Umbria-Marche arcuate fold belt (Italy), *Tectonophysics*, *146*, 125–137, doi:10.1016/0040-1951(88)90086-8.
- Lowrie, W., and A. Hirt (1988), Paleomagnetism in the arcuate mountain belts, *Tectonophysics*, *146*, 91–103.
- Marchegiani, L., G. Bertotti, G. Cello, G. Deiana, S. Mazzoli, and E. Tondi (1999), Pre-orogenic tectonics in the Umbria-Marche sector of the Afro-Adriatic continental margin, *Tectonophysics*, *315*(1–4), 123–143, doi:10.1016/S0040-1951(99)00277-2.
- Marshak, S., P. A. Geiser, W. Alvarez, and T. Engelder (1982), Mesoscopic fault array of the norther Umbria Apennine fold belt, Italy: Geometry of conjugate shear by pressure-solution slip, *Geol. Soc. Am. Bull.*, *93*(10), 1013–1022, doi:10.1130/0016-7606(1982)93<1013.

- Martinis, B., and M. Pieri (1964), Alcune notizie sulla formazione evaporitica dell'Italia centrale e meridionale, *Mem. Soc. Geol. Ital.*, *4*, 649–678.
- Mattei, M., R. Funicello, and C. Kissel (1995), Paleomagnetic and structural evidence for Neogene block rotations in the Central Apennines, Italy, *J. Geophys. Res.*, *100*, 17,863–17,883, doi:10.1029/95JB00864.
- Michael, A. J. (1984), Determination of stress from slip data: Faults and folds, *J. Geophys. Res.*, *89*, 11,517–11,526, doi:10.1029/JB089iB13p11517.
- Mirabella, F., M. R. Barchi, and A. Lupattelli (2008), Seismic reflection data in the Umbria Marche region: Limits and capabilities to unravel the subsurface structure in a seismically active area, *Ann. Geophys.*, *51*(2-3), 383–396, doi:10.4401/ag-3032.
- Mourgues, R., and P. Cobbold (2003), Some tectonic consequences of fluid overpressures and seepage forces as demonstrated by sandbox modelling, *Tectonophysics*, *376*(1-2), 75–97, doi:10.1016/S0040-1951(03)00348-2.
- Mourgues, R., and P. R. Cobbold (2006), Thrust wedges and fluid overpressures: Sandbox models involving pore fluids, *J. Geophys. Res.*, *111*, B05404, doi:10.1029/2004JB003441.
- Orife, T., and R. J. Lisle (2003), Numerical processing of palaeostress results, *J. Struct. Geol.*, *25*, 949–957, doi:10.1016/S0191-8141(02)00120-7.
- Orife, T., and R. J. Lisle (2006), Assessing the statistical significance of palaeostress estimates: Simulations using random fault-slips, *J. Struct. Geol.*, *28*, 952–956, doi:10.1016/j.jsg.2006.03.005.
- Park, W., and E. Schot (1968), Stylolites: Their nature and origin, *J. Sediment. Res.*, *38*, 175–191.
- Petit, J.-P., and M. Mattauer (1995), Paleostress superimposition deduced from mesoscale structures in limestone: The Matelles exposure, Languedoc, France, *J. Struct. Geol.*, *17*(2), 254–256.
- Petracchini, L., M. Antonellini, A. Billi, and D. Scrocca (2012), Fault development through fractured pelagic carbonates of the Cingoli anticline, Italy: Possible analog for subsurface fluid-conductive fractures, *J. Struct. Geol.*, *45*, 21–37, doi:10.1016/j.jsg.2012.05.007.
- Pierantoni, P., G. Deiana, and S. Galdenzi (2013), Stratigraphic and structural features of the Sibillini Mountains (Umbria-Marche Apennines, Italy), *Ital. J. Geosci.*, *132*(3), 497–520, doi:10.3301/IJG.2013.08.
- Pizzi, A., and V. Scisciani (2000), Methods for determining the Pleistocene-Holocene component of displacement on active faults reactivating pre-Quaternary structures: Examples from the Central Apennines (Italy), *J. Geodyn.*, *29*(3-5), 445–457, doi:10.1016/S0264-3707(99)00053-8.
- Pollard, D. D., and A. Aydin (1988), Progress in understanding jointing over the past century, *Geol. Soc. Am. Bull.*, *100*(8), 1181–1204, doi:10.1130/0016-7606(1988)100<1181:PIUJOT>2.3.CO;2.
- Quintà, A., and S. Tavani (2012), The foreland deformation in the south-western Basque-Cantabrian Belt (Spain), *Tectonophysics*, *576*–577, 4–19, doi:10.1016/j.tecto.2012.02.015.
- Railsback, L. B. (1993), Lithologic controls on morphology of pressure-dissolution surfaces (stylolites and dissolution seams) in Paleozoic carbonate rocks from the mideastern United States, *J. Sediment. Res.*, *63*(3), 513–522, doi:10.2110/jsr.63.513.
- Renard, F., J. Schmittbuhl, J.-P. Gratier, P. Meakin, and E. Merino (2004), Three-dimensional roughness of stylolites in limestones, *J. Geophys. Res.*, *109*, B03209, doi:10.1029/2003JB002555.
- Rocher, M., O. Lacombe, J. Angelier, and H.-W. Chen (1996), Mechanical twin sets in calcite as markers of recent collisional events in a fold-and-thrust belt: Evidence from the reefal limestones of southwestern Taiwan, *Tectonics*, *15*, 984–996, doi:10.1029/96TC00625.
- Rocher, M., O. Lacombe, J. Angelier, B. Deffontaines, and F. Verdier (2000), Cenozoic folding and faulting in the North Pyrenean Foreland (Aquitaine Basin, France): Insights from combined structural and paleostress analyses, *J. Struct. Geol.*, *22*(5), 627–645.
- Rocher, M., M. Cushing, F. Lemeille, Y. Lozac'h, and J. Angelier (2004), Intraplate paleostresses reconstructed with calcite twinning and faulting: Improved method and application to the eastern Paris Basin (Lorraine, France), *Tectonophysics*, *387*(1-4), 1–21, doi:10.1016/j.tecto.2004.03.002.
- Rolland, A., R. Toussaint, P. Baud, J. Schmittbuhl, N. Conil, D. Koehn, F. Renard, and J.-P. Gratier (2012), Modeling the growth of stylolites in sedimentary rocks, *J. Geophys. Res.*, *117*, B06403, doi:10.1029/2011JB009065.
- Rolland, A., R. Toussaint, P. Baud, N. Conil, and P. Landrein (2014), Morphological analysis of stylolites for paleostress estimation in limestones, *Int. J. Rock Mech. Min. Sci.*, *67*, 212–225, doi:10.1016/j.ijrmms.2013.08.021.
- Roure, F., et al. (2010), The use of palaeo-thermo-barometers and coupled thermal, fluid flow and pore-fluid pressure modelling for hydrocarbon and reservoir prediction in fold and thrust belts, *Geol. Soc. London Spec. Publ.*, *348*, 87–114.
- Rowe, K. J., and E. H. Rutter (1990), Palaeostress estimation using calcite twinning: Experimental calibration and application to nature, *J. Struct. Geol.*, *12*(1), 1–17, doi:10.1016/0191-8141(90)90044-Y.
- Saintot, A., R. Stephenson, A. Brem, S. Stovba, and V. Privalov (2003), Paleostress field reconstruction and revised tectonic history of the Donbas fold and thrust belt (Ukraine and Russia), *Tectonics*, *22*(5), 1059, doi:10.1029/2002TC001366.
- Savage, H. M., R. J. Shackleton, M. L. Cooke, and J. J. Riedel (2010), Insights into fold growth using fold-related joint patterns and mechanical stratigraphy, *J. Struct. Geol.*, *32*(10), 1466–1475, doi:10.1016/j.jsg.2010.09.004.
- Scarselli, S., G. D. H. Simpson, P. A. Allen, G. Minelli, and L. Gaudenzi (2007), Association between Messinian drainage network formation and major tectonic activity in the Marche Apennines (Italy), *Terra Nova*, *19*(1), 74–81, doi:10.1111/j.1365-3121.2006.00717.x.
- Schmittbuhl, J., F. Renard, J. Gratier, and R. Toussaint (2004), Roughness of stylolites: Implications of 3D high resolution topography measurements, *Phys. Rev. Lett.*, *93*(23), 238501, doi:10.1103/PhysRevLett.93.238501.
- Scisciani, V., S. Agostini, F. Calamita, P. Pace, A. Cilli, I. Giori, and W. Paltrinieri (2014), Positive inversion tectonics in foreland fold-and-thrust belts: A reappraisal of the Umbria-Marche Northern Apennines (Central Italy) by integrating geological and geophysical data, *Tectonophysics*, *637*, 218–237, doi:10.1016/j.tecto.2014.10.010.
- Speranza, F., L. Sagnotti, and M. Mattei (1997), Tectonics of the Umbria-Marche-Romagna Arc (central northern Apennines, Italy): New paleomagnetic constraints, *J. Geophys. Res.*, *102*, 3153–3166, doi:10.1029/96JB03116.
- Stearns, D. W., and M. Friedman (1972), Reservoirs in fractured rock, *Geol. Explor. Methods*, *10*, 82–106.
- Stockdale, P. B. (1943), Stylolites: Primary or secondary?, *J. Sediment. Res.*, *13*(1), 3–12, doi:10.1306/D4269175-2B26-11D7-864800102C1865D.
- Storti, F., and F. Salvini (2001), The evolution of a model trap in the central Apennines, Italy: Fracture patterns, fault reactivation and development of cataclastic rocks in carbonates at the Narni Anticline, *J. Pet. Geol.*, *24*(2), 171–190, doi:10.1111/j.1747-5457.2001.tb00666.x.
- Tavani, S., and F. Cifelli (2010), Deformation pattern analysis and tectonic implications of a décollement level within the Central Apennines (Italy), *Geol. J.*, *45*(5-6), 582–596, doi:10.1002/gj.1198.
- Tavani, S., F. Storti, F. Salvini, and C. Toscano (2008), Stratigraphic versus structural control on the deformation pattern associated with the evolution of the Mt. Catria anticline, Italy, *J. Struct. Geol.*, *30*, 664–681, doi:10.1016/j.jsg.2008.01.011.
- Tavani, S., F. Storti, J. Bausà, and J. A. Muñoz (2012), Late thrusting extensional collapse at the mountain front of the northern Apennines (Italy), *Tectonics*, *31*, TC4019, doi:10.1029/2011TC003059.
- Tavani, S., F. Storti, O. Lacombe, A. Corradetti, J. a. Muñoz, and S. Mazzoli (2015), A review of deformation pattern templates in foreland basin systems and fold-and-thrust belts: Implications for the state of stress in the frontal regions of thrust wedges, *Earth Sci. Rev.*, *141*, 82–104, doi:10.1016/j.earscirev.2014.11.013.

- Thomson, S. N., M. T. Brandon, P. W. Reiners, M. Zattin, P. J. Isaacson, and M. L. Balestrieri (2010), Thermochronologic evidence for orogen-parallel variability in wedge kinematics during extending convergent orogenesis of the northern Apennines, Italy, *GSA Bull.*, 122(7), 1160–1179, doi:10.1130/B26573.1.
- Tondi, E., M. Antonellini, A. Aydin, L. Marchegiani, and G. Cello (2006), The role of deformation bands, stylolites and sheared stylolites in fault development in carbonate grainstones of Majella Mountain, Italy, *J. Struct. Geol.*, 28(3), 376–391, doi:10.1016/j.jsg.2005.12.001.
- van Hinsbergen, D. J. J., M. Mensink, C. G. Langereis, M. Maffione, L. Spalluto, M. Tropeano, and L. Sabato (2014), Did Adria rotate relative to Africa?, *Solid Earth*, 5(2), 611–629, doi:10.5194/se-5-611-2014.
- Varga, R. J. (1993), Rocky Mountain foreland uplifts: Products of a rotating stress field or strain partitioning?, *Geology*, 21(12), 1115, doi:10.1130/0091-7613(1993)021<1115:RMFUPO>2.3.CO;2.
- Ventura, B., G. A. Pini, and G. G. Zuffa (2001), Thermal history and exhumation of the Northern Apennines (Italy): Evidence from combined apatite fission track and vitrinite reflectance data from foreland basin sediments, *Basin Res.*, 13, 435–448, doi:10.1046/j.0950-091X.2001.00159.x.
- Weil, A. B., and W. A. Yonkee (2012), Layer-parallel shortening across the Sevier fold-thrust belt and Laramide foreland of Wyoming: Spatial and temporal evolution of a complex geodynamic system, *Earth Planet. Sci. Lett.*, 357–358, 405–420, doi:10.1016/j.epsl.2012.09.021.
- Wright, K., R. T. Cygan, and B. Slater (2001), Structure of the (101 $\bar{4}$ ) surfaces of calcite, dolomite and magnesite under wet and dry conditions, *Phys. Chem. Chem. Phys.*, 3(5), 839–844, doi:10.1039/b006130l.
- Zattin, M. (1999), Apatite thermochronology of the Marnoso-arenacea succession (Miocene, Northern Apennines), Univ. of Bologna, *A compléter*.